pathogens

MDPI

Article

Potentiation of Rifampicin Activity Against Multidrug-Resistant *Klebsiella pneumoniae* by Green-Synthesized Zirconium Dioxide Nanoparticles: Preliminary Observations on Efflux, Gene Expression, and Biofilm Formation

Rehab A. Ibrahim [1,*], Abdulaziz M. Almuzaini [2], Eman Y. T. Elariny [1], Eman Marzouk [3,*] and Hadeer I. Abd Elbadie [1]

[1] Botany and Microbiology Department, Faculty of Science, Zagazig University, Zagazig 44519, Egypt; eytohamy@zu.edu.eg (E.Y.T.E.); hadeerhadeer965@gmail.com (H.I.A.E.)
[2] Department of Veterinary Preventive Medicine, College of Veterinary Medicine, Qassim University, Buraydah 51452, Saudi Arabia; ammzieny@qu.edu.sa
[3] Department of Public Health, College of Applied Medical Sciences, Qassim University, P.O. Box 6666, Buraydah 51452, Saudi Arabia
* Correspondence: rehabatef@yahoo.com (R.A.I.); e.marzouk@qu.edu.sa (E.M.); Tel.: +966-20-1065953211 (E.M.)

Abstract

Multidrug-resistant (MDR) *Klebsiella pneumoniae* excludes otherwise potent antibiotics such as rifampicin through its outer membrane and efflux systems. Zirconium dioxide (ZrO_2) nanoparticles were biosynthesized using *Salvia officinalis* leaf extract, characterized, and evaluated with rifampicin against three MDR *K. pneumoniae* clinical isolates. The fractional inhibitory concentration index was 0.375 in all three isolates, consistent with checkerboard synergy; in the most resistant isolate, PX285917, the rifampicin minimum inhibitory concentration (MIC) fell from 64 to 8 µg/mL. In time–kill assays the combination (32 + 8 µg/mL) was more active than either agent alone at every point from 2 h onwards ($p < 0.001$), reducing viable counts by 4.16 $\log_{10}$ colony-forming units (CFU)/mL relative to the control at 8 h; its advantage over the more active single agent reached 1.14 $\log_{10}$ CFU/mL, below the ≥2 $\log_{10}$ time–kill definition of synergy. In PX285917 the combination reduced biofilm formation by 92.59%, lowered *acrAB*, *ompK35* and *ompK36* expression by 90.6%, 78.5% and 68.2%, increased ethidium bromide retention (70.4% versus 39.0% at 15 min) and propidium iodide uptake (35.0% of the permeabilized reference), and caused extensive envelope damage. Biosynthesized ZrO_2 nanoparticles therefore restore rifampicin activity in vitro through increased membrane permeability and reduced efflux-gene expression.

Keywords: *Klebsiella pneumoniae*; antimicrobial resistance; zirconium dioxide nanoparticles; green synthesis; rifampicin; antibiotic adjuvant; synergy; efflux pump; biofilm

Check for updates

Academic Editor: Maria King

Received: 4 November 2026
Revised: 25 November 2026
Accepted: 26 November 2026
Published: 27 November 2026

Copyright: © 2026 by the authors. Licensee MDPI, Basel, Switzerland. This article is an open access article distributed under the terms and conditions of the Creative Commons Attribution (CC BY) license.

1. Introduction

Antimicrobial resistance (AMR) has become one of the most critical threats to global public health, compromising the effectiveness of antibiotic therapy and increasing the incidence of persistent infections, prolonged hospitalization, and mortality. According to the World Health Organization (WHO), multidrug-resistant (MDR) Gram-negative bacteria represent a critical priority for the development of novel therapeutic strategies, among which *Klebsiella pneumoniae* has emerged as one of the most problematic nosocomial pathogens because of its remarkable capacity to acquire and disseminate AMR

determinants [1,2]. This opportunistic bacterium is responsible for a broad spectrum of healthcare-associated infections, including pneumonia, urinary tract infections, bloodstream infections, wound infections, and sepsis, particularly among immunocompromised and critically ill patients [3–5].

Biofilm formation further complicates the treatment of *K. pneumoniae* infections by providing an additional layer of protection against antimicrobial agents and host immune defenses. Within the biofilm matrix, bacterial cells are embedded in a self-produced extracellular polymeric substance (EPS) that restricts antibiotic penetration, promotes horizontal transfer of resistance determinants, and facilitates the establishment of persistent and recurrent infections. Consequently, biofilm-associated *K. pneumoniae* infections frequently exhibit substantially greater antimicrobial tolerance than their planktonic counterparts, particularly in catheter-associated urinary tract infections, ventilator-associated pneumonia, bloodstream infections, and chronic wound infections [4]. Therefore, strategies capable of simultaneously suppressing bacterial growth and preventing biofilm formation are needed to improve the treatment of MDR *K. pneumoniae* infections.

The remarkable adaptability of *K. pneumoniae* results from the coexistence of multiple resistance mechanisms that collectively reduce antibiotic susceptibility. Among these, the AcrAB-TolC multidrug efflux system plays a central role by actively exporting structurally diverse antimicrobial agents, thereby lowering intracellular antibiotic concentrations below therapeutic levels [6,7]. In parallel, alterations in the major outer membrane porins OmpK35 and OmpK36 modify membrane permeability and contribute to reduced antibiotic uptake, further enhancing multidrug resistance [8,9]. The combined action of active drug efflux and decreased membrane permeability substantially limits the clinical efficacy of many antibiotics, emphasizing the urgent need for alternative therapeutic strategies capable of overcoming these resistance mechanisms.

Rather than relying exclusively on the discovery of new antimicrobial agents, increasing attention has been directed toward antibiotic adjuvant therapy, in which non-antibiotic compounds restore or enhance the activity of existing antibiotics by targeting bacterial resistance pathways [10,11]. This approach offers several potential advantages, including improved therapeutic efficacy, reduced antibiotic dosage, delayed emergence of resistance, and extension of the clinical lifespan of currently available antibiotics. Consequently, identifying safe and effective adjuvants capable of resensitizing MDR pathogens has become an important objective in antimicrobial research.

Rifampicin was selected as the partner antibiotic in this study for three related reasons. It is among the most potent inhibitors of bacterial DNA-dependent RNA polymerase and is well characterised, inexpensive and orally available [12–14]. Its activity against Gram-negative organisms is nevertheless limited, because the large, lipophilic molecule is largely excluded by the outer-membrane permeability barrier and what enters is removed by resistance–nodulation–division (RND)-family efflux pumps [6,7,15]; for this reason neither the Clinical and Laboratory Standards Institute (CLSI) nor the European Committee on Antimicrobial Susceptibility Testing (EUCAST) publishes interpretive breakpoints for rifampicin against Enterobacterales [16,17]. Rifampicin is therefore limited by precisely the two mechanisms that metal oxide nanoparticles have been reported to affect [10,11,18], which makes it an informative test case for adjuvant-mediated restoration of activity rather than an agent expected to be useful against *K. pneumoniae* on its own.

Metal oxide nanoparticles have emerged as promising antimicrobial materials owing to their unique physicochemical characteristics, including high surface-area-to-volume ratio, enhanced surface reactivity, and the ability to interact directly with bacterial cell envelopes [19–23]. Among the available synthetic approaches, plant-mediated green synthesis has attracted considerable interest because phytochemicals function as natural stabilizing

and capping agents, providing an environmentally friendly, cost-effective, and sustainable alternative to conventional chemical synthesis while improving nanoparticle biocompatibility [24,25]. Zirconium dioxide (ZrO_2) nanoparticles possess excellent physicochemical stability, chemical inertness, and favorable biocompatibility, making them attractive candidates for biomedical applications [26–28]. Although several studies have demonstrated the antibacterial activity of biosynthesized ZrO_2 nanoparticles (NPs), most investigations have primarily focused on nanoparticle synthesis, physicochemical characterization, and conventional antimicrobial evaluation. ZrO_2 NPs have been combined with antibiotics against *K. pneumoniae* in a few studies, with ceftazidime [29] and with other agents against *Escherichia coli* and *K. pneumoniae* [30]; an ampicillin-loaded SiO_2/ZrO_2 sol–gel material has also been described [31], and erythromycin has been loaded onto other metal-oxide platforms such as Ag–ZnO [32]. Their role as antibiotic adjuvants capable of modulating bacterial resistance mechanisms nevertheless remains insufficiently explored [10,26–28,33]. Consequently, increasing attention has shifted from the direct antibacterial activity of nanoparticles toward their application as antibiotic adjuvants capable of restoring the efficacy of existing antimicrobial agents.

Recent evidence indicates that metal oxide nanoparticles may influence bacterial physiology beyond direct growth inhibition through interactions with membrane integrity, oxidative stress pathways, and multidrug resistance systems [19,20,23]. Nevertheless, the potential of green-synthesized ZrO_2 NPs to potentiate rifampicin activity against MDR *K. pneumoniae*, in association with changes in resistance-associated gene expression and bacterial ultrastructure, has not been examined. Furthermore, studies integrating phenotypic susceptibility testing with molecular analysis of resistance determinants and ultrastructural characterization remain limited.

Therefore, the present study aimed to investigate the potential of biosynthesized ZrO_2 NPs to potentiate rifampicin activity against MDR *K. pneumoniae*. Specifically, the study evaluated antibacterial synergy, biofilm inhibition, expression of the resistance-associated genes *acrAB*, *ompK35*, and *ompK36*, ethidium bromide retention, and treatment-associated ultrastructural alterations.

2. Materials and Methods

Chemicals and reagents. Zirconium oxychloride octahydrate ($ZrOCl_2 \cdot 8H_2O$), rifampicin, ciprofloxacin, glycerol, glucose, crystal violet, glutaraldehyde, ethidium bromide (EtBr), phosphate-buffered saline (PBS), potassium phosphate, magnesium chloride, methanol, and absolute ethanol were purchased from Sigma-Aldrich (St. Louis, MO, USA) and supplied by El-Gomhouria Company for Pharmaceuticals (Zagazig, Egypt). Culture media (MacConkey agar, tryptic soy broth, and Mueller–Hinton agar and broth) were obtained from Oxoid (Thermo Fisher Scientific, Basingstoke, UK), as were the commercial antibiotic discs used throughout: ampicillin (10 µg), amoxicillin/clavulanic acid (20/10 µg), cefotaxime (30 µg), ceftazidime (30 µg), imipenem (10 µg), meropenem (10 µg), gentamicin (10 µg), ciprofloxacin (5 µg), tetracycline (30 µg), chloramphenicol (30 µg) and rifampicin (30 µg). Whatman No. 1 filter paper was obtained from Cytiva (Maidstone, UK). Fresh leaves of *Salvia officinalis* were obtained from the Faculty of Agriculture, Zagazig University, Zagazig, Egypt.

2.1. Source and Phenotypic Characterization of the Clinical Klebsiella pneumoniae Isolates

Three clinical bacterial isolates were obtained from the culture collection of the Department of Microbiology, Faculty of Science, Ain Shams University, Cairo, Egypt. According to the records of the collection, the isolates had been recovered and archived by that department from sputum, urine and pus specimens submitted for diagnostic purposes; they were

supplied to the present authors as anonymised bacterial cultures. Upon receipt, each isolate was subcultured on MacConkey agar (Oxoid, Basingstoke, UK) and incubated aerobically at 37 °C for 18–24 h to obtain fresh pure cultures. Colony morphology was recorded, and Gram staining was performed according to standard microbiological procedures to confirm the purity and Gram-negative characteristics of the isolates [34,35]. Pure cultures were maintained on MacConkey agar slants at 4 °C for routine use and preserved in tryptic soy broth (TSB; Oxoid, UK) supplemented with 20% (*v*/*v*) sterile glycerol at −80 °C for long-term storage.

2.2. Molecular Identification of Klebsiella pneumoniae Isolates

Genomic DNA was extracted from freshly cultured bacterial isolates using the QIAamp DNA Mini Kit (QIAGEN, Hilden, Germany) according to the manufacturer's instructions. Molecular identification was performed by amplification of the 16S rRNA gene using the universal bacterial primers 27F (5′-AGAGTTTGATCMTGGCTCAG-3′) and 1492R (5′-TACGGYTACCTTGTTACGACTT-3′) [36]. Polymerase chain reaction (PCR) amplification was carried out under standard thermal cycling conditions, and the amplified products were verified by electrophoresis on 1.5% agarose gel stained with EtBr.

The purified PCR products were commercially sequenced, and the resulting nucleotide sequences were compared with sequences available in the National Center for Biotechnology Information (NCBI) database using the Basic Local Alignment Search Tool (BLAST) algorithm, BLAST was run through the NCBI web service (National Center for Biotechnology Information, Bethesda, MD, USA) [37]. Sequence analysis confirmed that all three isolates belonged to *K. pneumoniae*. The obtained 16S rRNA gene sequences were subsequently deposited in the GenBank database under accession numbers PX285917, PX285918, and PX285919.

2.3. Antimicrobial Susceptibility Testing

The antimicrobial susceptibility profiles of the three *K. pneumoniae* isolates were determined using the Kirby–Bauer disk diffusion method on Mueller–Hinton agar (Oxoid, UK) according to CLSI guidelines [16]. Fresh bacterial suspensions were prepared in sterile physiological saline and adjusted to the turbidity of a 0.5 McFarland standard (approximately 1.5×10^8 colony-forming units (CFU) mL^{-1}). The standardized inoculum was uniformly spread over Mueller–Hinton agar plates using sterile cotton swabs.

Commercial antibiotic discs representing different antimicrobial classes were placed onto the inoculated agar surface. The eleven antibiotics tested included ampicillin (10 µg), cefotaxime (30 µg), meropenem (10 µg), ciprofloxacin (5 µg), gentamicin (10 µg), amoxicillin/clavulanic acid (20/10 µg), ceftazidime (30 µg), imipenem (10 µg), tetracycline (30 µg), chloramphenicol (30 µg), and rifampicin (30 µg). Following aerobic incubation at 37 °C for 18–24 h, inhibition zone diameters were measured and interpreted as susceptible, intermediate, or resistant according to CLSI breakpoints (CLSI M100, 35th edition (2025); Supplementary Table S1) [16]. Because CLSI M100 and EUCAST do not provide interpretive breakpoints for rifampicin against Enterobacterales, rifampicin zone diameters and MICs are reported as continuous, descriptive values only and were not assigned a formal susceptibility category. *E. coli* ATCC 25922 was included as the quality-control strain for the disc-diffusion tests.

Based on the obtained susceptibility profiles, the sputum isolate (GenBank accession number PX285917) exhibited the highest level of multidrug resistance and was selected as the representative MDR isolate for the mechanistic experiments; minimum inhibitory concentration, minimum bactericidal concentration and checkerboard assays were performed on all three isolates.

2.4. Preparation of Salvia Officinalis Aqueous Extract

Fresh leaves of *Salvia officinalis* were thoroughly washed with running tap water followed by deionized water to remove surface contaminants. The cleaned leaves were air-dried under shade at room temperature and ground into a fine powder using a laboratory-type mill (Moulinex, Groupe SEB, Écully, France). An aqueous extract was prepared by mixing 10 g of powdered leaves with 100 mL of deionized water, followed by heating at 60 °C for 2 h under continuous magnetic stirring.

This extraction procedure was performed according to previously published plant-mediated nanoparticle synthesis protocols [25,27,28]. The chemical composition of the extract was not profiled in this study; no gas chromatography–mass spectrometry (GC-MS) or liquid chromatography–mass spectrometry (LC-MS) analysis of the *S. officinalis* preparation was performed, so the individual constituents responsible for reduction and stabilization were not identified here.

2.5. Green Synthesis of ZrO_2 NPs

Biosynthesized zirconium dioxide nanoparticles (ZrO_2 NPs) were prepared using the aqueous extract of *S. officinalis* as a stabilizing and capping agent. Briefly, 10 mL of the plant extract was added dropwise to 90 mL of 0.01 M zirconium oxychloride octahydrate ($ZrOCl_2 \cdot 8H_2O$) under continuous magnetic stirring. The reaction mixture was maintained under stirring overnight at room temperature until the formation of a white precipitate, indicating successful nanoparticle formation.

The precipitate was collected by centrifugation (Eppendorf, Hamburg, Germany) at 12,000 rpm for 15 min, washed three times with deionized water followed by absolute ethanol to remove residual precursor salts and unbound phytochemicals, and dried overnight in a hot-air oven. The dried material was subsequently calcined in a muffle furnace at 500 °C for 4 h to obtain crystalline ZrO_2 NPs. The synthesized nanoparticles were stored in sterile airtight containers until physicochemical characterization and biological evaluation [27,28].

2.6. Physicochemical Characterization of Biosynthesized ZrO_2 NPs

The physicochemical properties of the biosynthesized ZrO_2 NPs were comprehensively characterized using multiple analytical techniques.

The optical properties of the synthesized nanoparticles were examined by ultraviolet–visible (UV–Vis) spectroscopy using a UV–Vis spectrophotometer (Shimadzu UV-2600i double-beam with an integrating sphere, Kyoto, Japan) over the wavelength range of 200–800 nm at a scan speed of 400 nm/min and a spectral bandwidth of 1.0 nm, using nanoparticle suspensions (0.1 mg/mL in deionized water) in 10 mm quartz cuvettes with deionized water as the reference. The optical band gap energy was subsequently estimated from the corresponding Tauc plot, assuming a direct allowed transition and extrapolating the linear region of $(\alpha h\nu)^2$ versus $h\nu$ (fitting range, 5.1–5.6 eV).

The morphology, particle size, and size distribution of the nanoparticles were investigated using transmission electron microscopy (TEM; JEOL JEM-2100F, Tokyo, Japan) operated at an accelerating voltage of 200 kV [38]. A dilute suspension of the nanoparticles in ethanol (0.05 mg/mL) was ultrasonicated for 15 min, and a drop was deposited on a 300-mesh carbon-coated copper grid (Ted Pella, Inc., Redding, CA, USA) and dried at ambient conditions. Particle diameters were measured from TEM micrographs using ImageJ software (v1.54f; National Institutes of Health, Bethesda, MD, USA), for at least 140 individual particles from multiple micrographs, and the size distribution was fitted to a log-normal function.

The crystalline structure of the nanoparticles was analyzed by X-ray diffraction (XRD) using a Bruker D8 Advance diffractometer (Bruker AXS GmbH, Karlsruhe, Germany) operating in Bragg–Brentano geometry with Cu-Kα radiation (λ = 1.5406 Å) at 40 kV and 40 mA. Diffraction patterns were recorded over a 2θ range of 10–80° with a step size of 0.01° and a scan rate of 2°/min, and crystalline phases were identified by comparison with the ICDD PDF-4+ database using DIFFRAC.EVA software Version 7.0. The average crystallite size (D) was estimated using the Scherrer equation, $D = K\lambda/(\beta \cos \theta)$, where K is the shape factor (0.9), β is the full width at half maximum (FWHM) corrected for instrumental broadening using a LaB_6 standard (NIST SRM 660c), and θ is the Bragg angle [39,40]. The calculation was based on the most intense (−111) reflection at 2θ = 28.17° (Supplementary Table S2).

Functional groups involved in nanoparticle synthesis and stabilization were identified by Fourier-transform infrared spectroscopy (FTIR) using a Bruker VERTEX 70 FTIR spectrometer (Bruker Optics GmbH & Co. KG, Ettlingen, Germany) equipped with a DTGS detector and a KBr beamsplitter. Spectra were recorded over the range of 4000–400 cm^{-1} at a spectral resolution of 4 cm^{-1} with 64 co-added scans. Samples were prepared by the KBr pellet technique (nanoparticle powder mixed with spectroscopic-grade KBr at 1:100, *w*/*w*, and pressed at 10 tons), a pure KBr pellet served as the background, and the optical bench was purged with dry, CO_2-free air.

Hydrodynamic particle size, polydispersity index (PDI), and zeta potential were determined by dynamic light scattering (DLS) using a Zetasizer Nano ZS (Malvern Panalytical Ltd., Malvern, UK). Measurements were performed at 25 °C using freshly dispersed nanoparticle suspensions prepared in deionized water. Nanoparticle dispersions (0.1 mg/mL) were ultrasonicated for 10 min before analysis. DLS was performed with a He–Ne laser (λ = 633 nm) at a scattering angle of 173° (backscatter) in disposable polystyrene cuvettes, and the Z-average diameter and PDI were obtained by cumulants analysis (ISO 22412:2017). Zeta potential was measured in folded capillary cells (DTS1070) by M3-PALS. All measurements were performed in triplicate, and the results are reported as the mean ± standard deviation (SD).

Elemental composition was determined by energy-dispersive X-ray spectroscopy (EDX) using an EDAX APEX system (EDAX Inc., Mahwah, NJ, USA) coupled to a field-emission scanning electron microscope (FE-SEM; JEOL, Tokyo, Japan) operated at 20 kV with a silicon drift detector (take-off angle, 35°; live time, 60 s). Powders were mounted on carbon tape and coated with a thin (~10 nm) carbon layer, and quantification was performed by the standardless eZAF (ZAF matrix correction) method [41].

Thermal stability was evaluated by thermogravimetric analysis (TGA) using a TGA Q500 analyzer (TA Instruments, New Castle, DE, USA). Approximately 10 mg of nanoparticle powder in an alumina crucible was heated from room temperature to 900 °C under a nitrogen atmosphere (flow rate, 60 mL min^{-1}) at a heating rate of 10 °C min^{-1}. The temperature was calibrated with the Curie point of nickel, and weight-loss (TGA) and derivative thermogravimetry (DTG) curves were recorded simultaneously (ASTM E1131).

2.7. Evaluation of the Antibacterial Activity of ZrO_2 NPs

Two diffusion assays were used, for different purposes. Disc diffusion with the full eleven-agent antibiotic panel served as a qualitative screen, to identify which antibiotics showed enhanced activity when combined with the nanoparticles. Agar well diffusion was then used as the quantitative, concentration-ranged comparison of the nanoparticles, rifampicin and their combination. Both were performed according to CLSI guidelines [16].

Fresh bacterial cultures were grown overnight in Mueller–Hinton broth (Oxoid, UK) at 37 °C and adjusted to a turbidity equivalent to a 0.5 McFarland standard (approximately

1.5×10^8 CFU mL^{-1}). The standardized bacterial suspension was uniformly spread onto Mueller–Hinton agar plates using sterile cotton swabs.

Sterile paper discs (6 mm diameter) were impregnated with ZrO_2 NPs (100 µL per disc; 100 µg/mL) and placed onto the inoculated agar surface. Commercial antibiotic discs representing different antimicrobial classes were simultaneously tested individually and in combination with ZrO_2 NPs to evaluate potential synergistic antibacterial activity. The antibiotic discs used in this screening step were the same eleven-agent panel described above. Plates were incubated aerobically at 37 °C for 18–24 h, after which inhibition zone diameters were measured in millimeters.

Agar well diffusion. For quantitative comparison, wells (6 mm diameter) were punched into Mueller–Hinton agar plates inoculated as described above. Each well received a total volume of 100 µL: ZrO_2 NPs at 25, 50 or 100 µg/mL, rifampicin at 100 µg/mL, or, for the combination, 100 µL of a solution in which the two agents had been premixed so that each was present at the same concentration as in its own single-agent well (rifampicin 100 µg/mL plus ZrO_2 NPs 100 µg/mL); neither agent was therefore diluted by the combination. The stated values are the concentrations of the solutions loaded into the wells; the concentration reached within the agar is governed by diffusion and was not defined. Plates were incubated aerobically at 37 °C for 18–24 h, and inhibition zone diameters were measured in millimeters (mean ± SD of three independent experiments).

Of the eleven agents tested in combination with the nanoparticles, rifampicin showed the greatest enhancement of antibacterial activity, and it was therefore carried forward into all subsequent mechanistic investigations.

Determination of Minimum Inhibitory Concentration (MIC) and Minimum Bactericidal Concentration (MBC)

The MIC of ZrO_2 NPs, rifampicin, and their combination was determined using the broth microdilution method in sterile 96-well microplates according to CLSI recommendations [16].

Serial two-fold dilutions of each treatment were prepared in Mueller–Hinton broth to obtain the desired concentration range (2–256 µg/mL for both ZrO_2 NPs and rifampicin). Each well was inoculated with approximately 5×10^5 CFU mL^{-1} of each of the three clinical *K. pneumoniae* isolates (PX285917, PX285918 and PX285919) and incubated at 37 °C for 18–24 h.

The MIC was defined as the lowest concentration that completely inhibited visible bacterial growth. To determine the MBC, aliquots from wells showing no visible growth were subcultured onto Mueller–Hinton agar plates and incubated for an additional 24 h. The MBC was recorded as the lowest concentration that produced no bacterial colony growth on the agar surface. MIC and MBC determinations were performed in three independent experiments for each isolate; the modal value is reported, together with the range when the replicates differed by one twofold dilution. To assess the contribution of the green-synthesis route, three control materials were tested against isolate PX285917 under identical conditions: the *S. officinalis* aqueous extract (0.125–16 mg/mL), the zirconium precursor $ZrOCl_2 \cdot 8H_2O$ (8–1024 µg/mL), and commercially available chemically synthesized ZrO_2 (Sigma-Aldrich, zirconium(IV) oxide, CAS 1314-23-4, nanopowder, catalogue no. 544760; supplier-stated particle size < 100 nm by TEM) (8–512 µg/mL), each in three independent experiments.

2.8. Evaluation of the Synergistic Interaction Between ZrO_2 NPs and Rifampicin

The interaction between biosynthesized ZrO_2 NPs and rifampicin was assessed using the checkerboard broth microdilution method. Serial two-fold dilutions of ZrO_2 NPs

were prepared along one axis of sterile 96-well microplates, whereas serial dilutions of rifampicin were prepared along the perpendicular axis to generate all possible concentration combinations (2–256 µg/mL for both agents). The assay was performed against all three clinical isolates (PX285917, PX285918 and PX285919) in three independent experiments per isolate.

Following inoculation with the standardized bacterial suspension, microplates were incubated at 37 °C for 24 h. The fractional inhibitory concentration index (FICI) was calculated according to the following equations:

$$\text{FIC of } ZrO_2 \text{ NPs} = \text{MIC of } ZrO_2 \text{ in combination/MIC of } ZrO_2 \text{ alone}$$

$$\text{FIC of rifampicin} = \text{MIC of rifampicin in combination/MIC of rifampicin alone}$$

$$\text{FICI} = \text{FIC}(ZrO_2) + \text{FIC}(\text{rifampicin})$$

Interactions were interpreted as follows: FICI $\leq$ 0.5 indicated synergism; 0.5 < FICI $\leq$ 1.0 indicated an additive effect; 1.0 < FICI $\leq$ 4.0 indicated indifference; and FICI > 4.0 indicated antagonism [42].

2.9. Time–Kill Kinetic Assay

Time–kill kinetics were determined for the MDR *K. pneumoniae* isolate PX285917. An overnight culture was diluted in Mueller–Hinton broth to a starting density of approximately 5×10^5 CFU/mL. The viable count of the standardized inoculum was determined at the time of inoculation and this value was used as the 0 h count for all arms of the experiment. Four conditions were prepared in parallel: an untreated growth control, biosynthesized ZrO_2 NPs at 32 µg/mL, rifampicin at 8 µg/mL, and the two agents combined at the same concentrations, corresponding to the combination concentrations identified in the checkerboard assay.

Cultures were incubated at 37 °C and aliquots were withdrawn at 0, 2, 4, 6, 8 and 24 h. Each aliquot was serially ten-fold diluted in sterile saline and plated onto Mueller–Hinton agar. Colonies were enumerated after incubation at 37 °C for 18–24 h and viable counts were expressed as $\log_{10}$ CFU/mL. The assay was performed with three independent biological replicates. Synergy was defined as a decrease of $\geq$2 $\log_{10}$ CFU/mL for the combination relative to the most active single agent at 24 h, and bactericidal activity as a decrease of $\geq$3 $\log_{10}$ CFU/mL relative to the initial inoculum. Differences between the combination and the more active single agent at each sampling point were assessed by Welch's *t*-test.

2.10. Biofilm Inhibition Assay by Crystal Violet Microtiter Plate Method

The antibiofilm activity of biosynthesized ZrO_2 NPs, rifampicin, and their combination was evaluated using the crystal violet microtiter plate (MTP) assay. Overnight bacterial cultures were diluted in TSB supplemented with 1% glucose to obtain a final concentration of approximately 1×10^6 CFU/mL. Aliquots of 100 µL of the bacterial suspension were dispensed into sterile flat-bottom 96-well microplates, followed by the addition of 100 µL of the respective treatment solutions. Experimental groups included ZrO_2 NPs alone, rifampicin alone, and a combination of ZrO_2 NPs with rifampicin at the following final concentrations: ZrO_2 NPs, 150 µg/mL; rifampicin, 64 µg/mL; combination, 32 µg/mL ZrO_2 plus 8 µg/mL rifampicin. Untreated bacterial cultures served as the negative control, whereas ciprofloxacin-treated cultures were included as the positive control. Sterile medium without bacteria served as the blank.

The microplates were incubated statically at 37 °C for 24 h to allow biofilm formation. Following incubation, planktonic cells were carefully removed, and each well was gently washed three times with sterile PBS (pH 7.4) to remove non-adherent cells. The attached biofilms were fixed with 200 µL methanol for 15 min, after which the methanol was discarded

and the plates were air-dried. The fixed biofilms were stained with 0.1% (*w*/*v*) crystal violet for 15 min at room temperature. Excess stain was removed by thoroughly rinsing the wells with distilled water, and the plates were allowed to dry completely. To assess activity against established biofilms, a separate experiment was performed in which biofilms were first allowed to form from an inoculum of 1×10^6 CFU/mL in tryptic soy broth supplemented with 1% glucose for 24 h at 37 °C. Planktonic cells were then removed and the preformed biofilms were exposed for a further 24 h to ZrO_2 NPs (32 µg/mL), rifampicin (8 µg/mL) or their combination (32 + 8 µg/mL). Remaining biomass was quantified by crystal violet staining as described above, in three independent experiments.

The bound crystal violet was subsequently solubilized with 200 µL of 95% ethanol for 15 min, and the optical density (OD) was measured at 590 nm using a microplate reader (BioTek Instruments, Winooski, VT, USA). The percentage of biofilm inhibition was calculated according to the following equation:

$$\text{Biofilm inhibition (\%)} = [(\text{OD_control} - \text{OD_treated})/\text{OD_control}] \times 100$$

To establish whether the reduction in biofilm biomass was separable from growth inhibition, which requires concentrations below the planktonic MIC, the crystal-violet assay was also performed at sub-inhibitory concentrations of each agent (ZrO_2 NPs, 64 µg/mL; rifampicin, 32 µg/mL; and the two agents combined at those same concentrations). This experiment was performed separately from the main assay, using an initial inoculum of 1×10^7 CFU/mL rather than the 1×10^6 CFU/mL of the main assay, so that sufficient biofilm biomass would form for quantification under sub-inhibitory conditions; all other conditions were identical. At these concentrations, viable biofilm cells were additionally quantified: after the planktonic cells were removed and the wells were washed with PBS, the adherent biofilm was detached by scraping, resuspended in sterile PBS, serially diluted, and plated on Mueller–Hinton agar, and colonies were counted after incubation at 37 °C for 24 h (CFU/mL).

2.11. Quantitative Real-Time PCR (RT-qPCR) Analysis of Resistance-Associated Genes

The expression of antibiotic resistance-associated genes was evaluated by quantitative real-time PCR (RT-qPCR) in four parallel arms: an untreated control, ZrO_2 NPs alone (32 µg/mL), rifampicin alone (8 µg/mL) and the two agents in combination (32 + 8 µg/mL). All arms used the same exposure time (24 h at 37 °C) and all were compared with the same untreated control.

The selected MDR *K. pneumoniae* PX285917 isolate was grown in Mueller–Hinton broth and treated with the ZrO_2 nanoparticle–rifampicin combination at the combination concentrations determined by the checkerboard assay (ZrO_2 NPs, 32 µg/mL, plus rifampicin, 8 µg/mL). Untreated bacterial cultures served as the control. Following incubation for 24 h at 37 °C, total RNA was extracted using the RNeasy Mini Kit (QIAGEN, Hilden, Germany), after stabilization of the cells with RNAprotect Bacteria Reagent (QIAGEN) and lysozyme treatment (1 mg/mL in TE buffer), with on-column RNase-free DNase digestion according to the manufacturer's instructions. RNA purity and concentration were determined spectrophotometrically using a NanoDrop™ 2000 spectrophotometer (Thermo Fisher Scientific, Waltham, MA, USA). Samples with an A260/A280 ratio between 1.8 and 2.1 were used for subsequent analysis.

One-step RT-qPCR was performed in 25 µL reactions containing 12.5 µL of 2× Quanti-Tect SYBR Green PCR Master Mix (QIAGEN), 0.25 µL of RevertAid Reverse Transcriptase (200 U/µL; Thermo Fisher Scientific, Waltham, MA, USA), 20 pmol of each forward and reverse primer, 8.25 µL of RNase-free water, and 3 µL of template RNA, in a Stratagene Mx3005P real-time PCR system (Agilent Technologies, Santa Clara, CA, USA). Cycling

conditions were reverse transcription at 50 °C for 30 min and initial denaturation at 94 °C for 15 min, followed by 40 cycles of 94 °C for 15 s, annealing for 30 s (*ompK35* and *ompK36*, 60 °C; *acrAB*, 50 °C; reference gene, 55 °C) and extension at 72 °C for 30 s, followed by a dissociation (melting-curve) step. The primer pairs for *ompK35* and *ompK36* were designed for the present study and checked by Primer-BLAST against the *K. pneumoniae* HS11286 reference genome (NC_016845.1), which predicted a single amplicon for each pair. The *acrAB* primer pair was that of Wasfi et al. [43], and the *K. pneumoniae* 16S–23S rRNA internal transcribed spacer (ITS), which served as the reference gene for normalization, was amplified with the primers of Liu et al. [44]. Primer sequences and amplicon sizes are provided in Supplementary Table S3. Amplification efficiencies were not determined experimentally (no standard curves were run); the comparative $2^{-\Delta\Delta Ct}$ method therefore assumes comparable, near-optimal efficiencies for the target and reference primer pairs, and melting-curve analysis showed a single peak for each target, confirming single-product amplification (Supplementary Figure S5), and Primer-BLAST analysis of each primer pair against the *K. pneumoniae* HS11286 genome predicted a single amplicon (Supplementary Table S3); representative amplification plots are shown in Supplementary Figure S7. The primer pair designated *acrAB* [43] amplifies a 312-bp fragment within the *acrA* coding sequence of the *acrAB* operon (Supplementary Table S3). Because *acrA* and *acrB* are co-transcribed, *acrA* transcript abundance was used as a proxy for *acrAB* operon expression; *acrB* was not quantified separately.

Relative gene expression levels were calculated using the comparative $2^{-\Delta\Delta Ct}$ method. Gene expression was assessed in untreated cells and after treatment with ZrO_2 NPs alone, rifampicin alone and their combination, using the same concentrations and exposure time in every arm (ZrO_2 NPs, 32 µg/mL; rifampicin, 8 µg/mL; 24 h at 37 °C); all treatments were compared with the same untreated control. Reactions were performed on three independent biological replicates, each run in technical triplicate (the individual Ct values are given in Supplementary Table S5), and ΔCt values were used for statistical analysis [45].

2.12. EtBr Retention Assay

Intracellular accumulation and retention of EtBr were measured in MDR *K. pneumoniae* PX285917 by a fluorometric retention assay adapted from previously described methods [46,47]. Cells were grown in Mueller–Hinton broth at 37 °C to an optical density at 600 nm (OD_{600}) of approximately 0.6, harvested by centrifugation at 8000× *g* for 10 min at 4 °C, washed twice in 20 mM potassium phosphate buffer containing 1 mM $MgCl_2$ (hereafter PPB) and resuspended in PPB to an OD_{600} of 0.4. EtBr was added to a final concentration of 5 µM and the suspension was incubated at 20 °C with shaking at 150 rpm for 60 min to allow accumulation. Cells were then collected at 8000× *g* for 10 min, resuspended in PPB containing 5% (*w*/*v*) glucose to energize efflux, and dispensed in 200 µL aliquots into black flat-bottom 96-well plates. Fluorescence was recorded every 2.5 min for 15 min (excitation 530 nm, emission 590 nm) using a fluorescence microplate reader (BioTek Instruments, Winooski, VT, USA), and retention was expressed as relative fluorescence (%) of each sample's initial value. Five treatment arms were prepared in parallel and added 5 min before glucose energization: ZrO_2 NPs (32 µg/mL), rifampicin (8 µg/mL), the two agents in combination (32 + 8 µg/mL), the efflux inhibitor carbonyl cyanide m-chlorophenylhydrazone (CCCP; 50 µM in dimethyl sulfoxide (DMSO), final solvent concentration 0.5% *v*/*v*) as a positive control for efflux inhibition, and CCCP together with ZrO_2 NPs; untreated cells served as the negative control. All determinations were performed in three independent experiments.

2.13. Propidium Iodide Uptake Assay

Membrane integrity was assessed in parallel with the EtBr assay, in MDR *K. pneumoniae* PX285917, under the same treatment concentrations, pre-incubation and recording periods and in the same buffer. Propidium iodide (PI) was added from a 1 mg/mL stock to a final concentration of 10 μg/mL and the cells were stained for 15 min at room temperature, protected from light. Cells permeabilized with cetyltrimethylammonium bromide (CTAB; 300 μM for 15 min) served as the fully permeabilized reference (100%), and PI signals are expressed as a percentage of that reference. Determinations were performed in three independent experiments.

To exclude ZrO_2-induced fluorescence scattering or quenching, no-cell blanks containing EtBr with ZrO_2 NPs (32 μg/mL), rifampicin (8 μg/mL) or their combination were recorded under the same conditions (Supplementary Table S4). Cell viability under the assay conditions was assessed by viable counts (CFU/mL) after an exposure equal in duration to the assay itself, that is, the 5 min pre-incubation with the treatments followed by the 15 min recording period, and OD_{600} was recorded at the start and at the end of that period (Supplementary Table S4).

2.14. Scanning Electron Microscopy (SEM)

Morphological alterations induced by ZrO_2 NPs, rifampicin, and their combination were examined using scanning electron microscopy (SEM; JEOL, Tokyo, Japan).

Untreated bacterial cells and treated cultures (treated with ZrO_2 NPs at 128 μg/mL, rifampicin at 64 μg/mL, or the combination at 32 + 8 μg/mL) were harvested by centrifugation at 8000× *g* for 10 min and washed twice with PBS (pH 7.2). The bacterial pellets were fixed in 2.5% (*v*/*v*) glutaraldehyde at 4 °C for 2 h, followed by washing with PBS. Samples were subsequently dehydrated through a graded ethanol series (30%, 50%, 70%, 80%, 90%, 95%, and 100%), with each dehydration step performed for 10 min.

The dehydrated samples were air-dried, mounted on aluminum stubs using conductive carbon tape, sputter-coated with a thin layer of gold, and examined by SEM. Representative micrographs were recorded to compare the ultrastructural morphology of untreated cells with those exposed to rifampicin, ZrO_2 NPs, and the combined treatment.

2.15. Statistical Analysis

All experiments were performed in triplicate unless otherwise stated, and the results are presented as the mean ± SD.

Statistical analyses were conducted using GraphPad Prism version 9.0 (GraphPad Software Inc., San Diego, CA, USA). Data normality was evaluated using the Shapiro–Wilk test, while homogeneity of variances was assessed using Levene's test before statistical comparisons.

Differences among multiple experimental groups were analyzed using one-way analysis of variance (ANOVA), followed by Tukey's multiple comparison test. Relative gene expression data obtained by RT-qPCR were analyzed using the $2^{-\Delta\Delta Ct}$ method, and statistical comparisons between control and treated groups were performed separately for each gene on ΔCt values using Welch's *t*-test (n = 3 biological replicates per group).

Differences were considered statistically significant at $p < 0.05$.

3. Results

3.1. Antibiotic Susceptibility Profiling and Hierarchical Clustering of MDR Klebsiella pneumoniae Isolates

The antibiotic susceptibility profiles of the three molecularly identified *K. pneumoniae* isolates (PX285917, PX285918, and PX285919) were evaluated against eleven clinically

relevant antimicrobial agents using the Kirby–Bauer disc diffusion method. The resulting inhibition zone diameters were subjected to hierarchical clustering analysis to identify the isolate exhibiting the highest level of multidrug resistance (Figure 1).

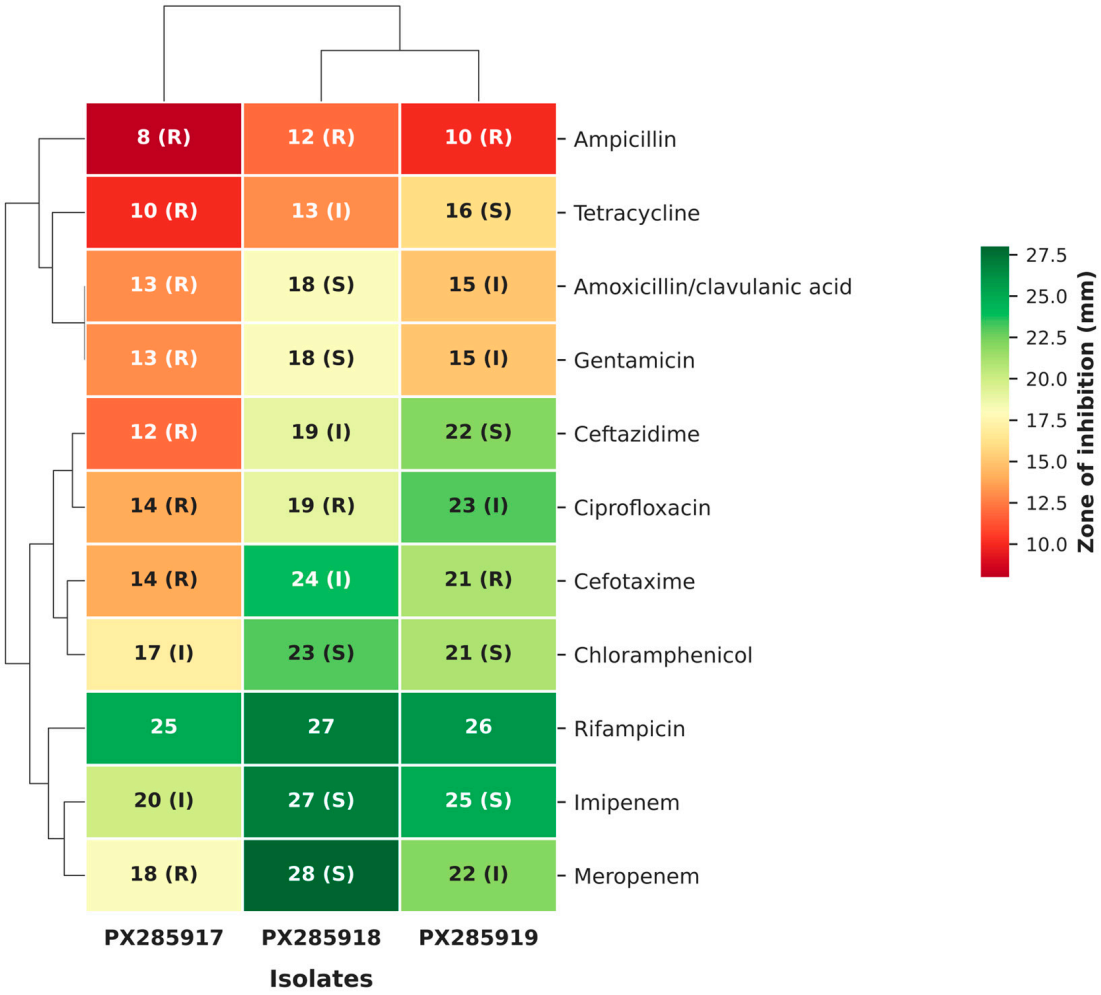


Figure 1. Heatmap and hierarchical clustering analysis of antibiotic susceptibility profiles of three molecularly identified *Klebsiella pneumoniae* isolates (PX285917, PX285918, and PX285919). The two-colour scale encodes inhibition zone diameters in millimetres, running from red (smallest zones) through to green (largest); the numerical values are given in Supplementary Table S1. The scale illustrates differences in antimicrobial susceptibility and the MDR phenotype of isolate PX285917. Rifampicin zone diameters are shown as continuous values only, because no CLSI or EUCAST interpretive breakpoints exist for rifampicin against Enterobacterales; S/I/R categories are shown for the other agents.

The heat map and dendrogram revealed two distinct susceptibility clusters. Isolate PX285917 formed an independent cluster, reflecting a pronounced MDR phenotype, whereas isolates PX285918 and PX285919 clustered closely together owing to their comparatively higher susceptibility to several antimicrobial agents.

Among the three isolates, PX285917 exhibited the lowest susceptibility to multiple antibiotic classes, including β-lactams and fluoroquinolones. Inhibition zone diameters of only 8 mm and 13 mm were observed for ampicillin and amoxicillin/clavulanic acid, respectively, while third-generation cephalosporins showed limited activity, with inhibition zones of 14 mm for cefotaxime and 12 mm for ceftazidime. Reduced susceptibility was also observed for gentamicin (13 mm) and ciprofloxacin (14 mm), confirming the MDR nature of this isolate.

Applying the criterion of non-susceptibility (intermediate or resistant) to at least one agent in three or more antimicrobial categories, all three isolates were classified as MDR. PX285917 was non-susceptible in eight categories (penicillins, β-lactam/β-lactamase-inhibitor combinations, extended-spectrum cephalosporins, carbapenems, aminoglycosides, fluoroquinolones, tetracyclines and phenicols), PX285919 in six (penicillins, β-lactam/β-lactamase-inhibitor combinations, extended-spectrum cephalosporins, carbapenems, aminoglycosides and fluoroquinolones) and PX285918 in four (penicillins, extended-spectrum cephalosporins, fluoroquinolones and tetracyclines). Categories were assigned from the measured zone diameters using the CLSI breakpoints listed in Supplementary Table S1 (Figure 1). The clear separation of PX285917 from the remaining isolates confirms its distinct resistance profile and supports its selection as the representative MDR strain for all subsequent antibacterial, molecular, and ultrastructural investigations.

3.2. Green Synthesis and Physicochemical Characterization of Biosynthesized ZrO_2 NPs

The biosynthesized ZrO_2 NPs were comprehensively characterized using transmission electron microscopy (TEM), X-ray diffraction (XRD), Fourier-transform infrared spectroscopy (FTIR), ultraviolet–visible (UV–Vis) spectroscopy, dynamic light scattering (DLS), zeta potential analysis, energy-dispersive X-ray spectroscopy (EDX), and thermogravimetric analysis (TGA) to evaluate their morphological, structural, optical, physicochemical, and thermal properties.

3.2.1. Morphological Characterization

TEM analysis demonstrated that the biosynthesized ZrO_2 NPs possessed predominantly quasi-spherical morphology with relatively uniform size distribution and smooth particle surfaces (Figure 2A). Slight particle agglomeration was observed, which is commonly associated with the high surface energy of metal oxide nanoparticles. Particle size analysis of 144 individual nanoparticles measured from the micrographs revealed a unimodal log-normal distribution with a mean particle diameter of 27.3 ± 12.6 nm and a median diameter of 24.2 nm (Figure 2B). Most nanoparticles ranged between 15 and 40 nm, while only a small proportion reached approximately 60 nm, indicating good control over nanoparticle nucleation and growth during the biosynthesis process.

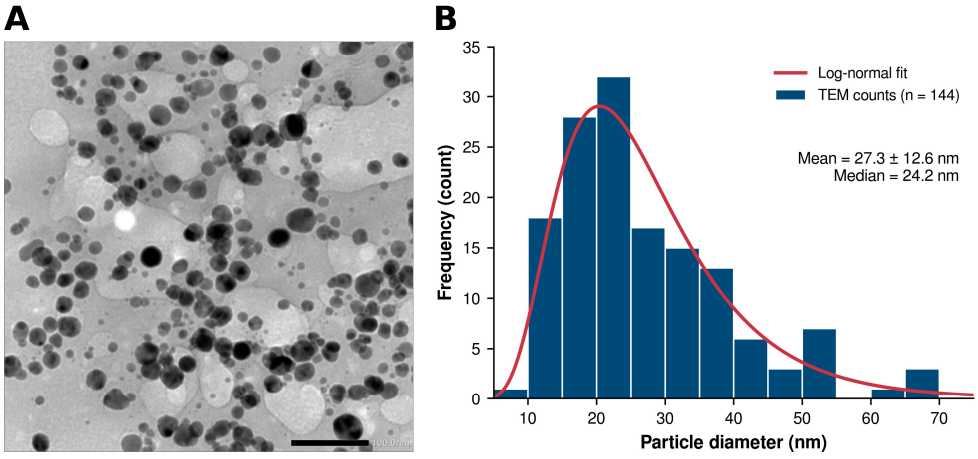


Figure 2. Morphology and size distribution of the biosynthesized ZrO_2 NPs. (**A**) Representative transmission electron micrograph (scale bar, 100 nm) showing quasi-spherical particles with smooth surfaces and slight agglomeration. (**B**) Particle size distribution obtained by measuring 144 individual particles from the micrographs, with a log-normal fit; mean diameter 27.3 ± 12.6 nm, median 24.2 nm.

3.2.2. Crystal Structure

The crystalline structure of the synthesized nanoparticles was confirmed by XRD analysis (Figure 3). The observed diffraction peaks were indexed to the monoclinic phase of zirconia (baddeleyite) and matched the reference pattern for monoclinic ZrO_2 (JCPDS/ICDD PDF No. 37-1484). The strongest diffraction peak was observed at $2\theta = 28.17°$, corresponding to the (−111) crystal plane, while additional reflections at 24.05°, 31.47°, 34.16°, 49.27°, and 50.12° were assigned to the (110), (111), (002), (−212), and (220) planes, respectively. The absence of detectable reflections attributable to tetragonal or cubic ZrO_2 indicates that the material predominantly consisted of the monoclinic phase.

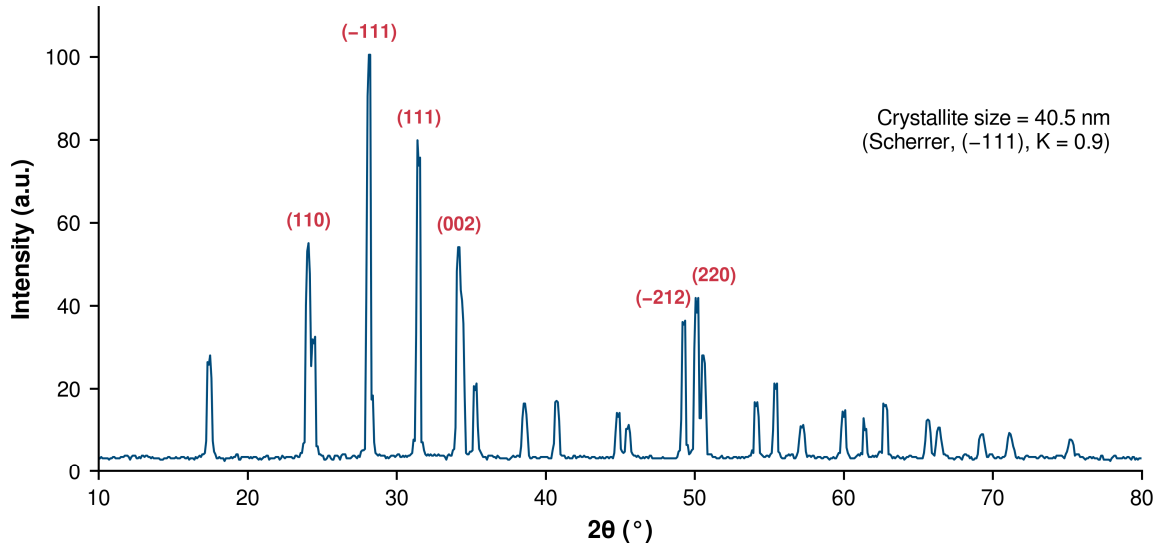


Figure 3. XRD pattern of ZrO_2 NPs indexed to the monoclinic phase (JCPDS 37-1484) with Miller indices annotated for major reflections.

The average crystallite size calculated using the Scherrer equation was approximately 40.5 nm ($D = K\lambda/\beta \cos\theta$; $K = 0.9$, $\lambda = 1.5406$ Å), calculated from the most intense (−111) reflection at $2\theta = 28.17°$, whose observed FWHM was 0.221°; the crystallite size was calculated from the FWHM after correction for instrumental broadening with the LaB_6 standard (Supplementary Table S2). This value is of the same order as the mean particle diameter determined by TEM (27.3 ± 12.6 nm). The slightly larger XRD value is reasonable because XRD gives a volume-weighted average that is dominated by the larger crystallites, whereas the TEM mean is number-weighted (n = 144 particles). As the two techniques measure different quantities, this agreement is regarded as reasonable and is not taken as evidence that the nanoparticles are single crystalline.

3.2.3. FTIR Analysis

FTIR spectra confirmed the successful formation of ZrO_2 NPs (Figure 4). Characteristic absorption bands located at 495, 580, and 745 cm^{-1} were assigned to Zr–O and Zr–O–Zr stretching vibrations, confirming the formation of the monoclinic zirconia lattice. Broad absorption bands centered at 3420 cm^{-1} and 1635 cm^{-1} corresponded to surface hydroxyl groups and adsorbed water molecules, whereas weaker bands at 1385 cm^{-1} and 1540 cm^{-1} were attributed to surface carbonate species. The absorption band at 1050 cm^{-1} indicated the presence of surface Zr–OH groups; however, because the material was calcined at 500 °C, this spectrum alone cannot show whether phytochemical constituents of the plant extract remained adsorbed on the nanoparticle surface.

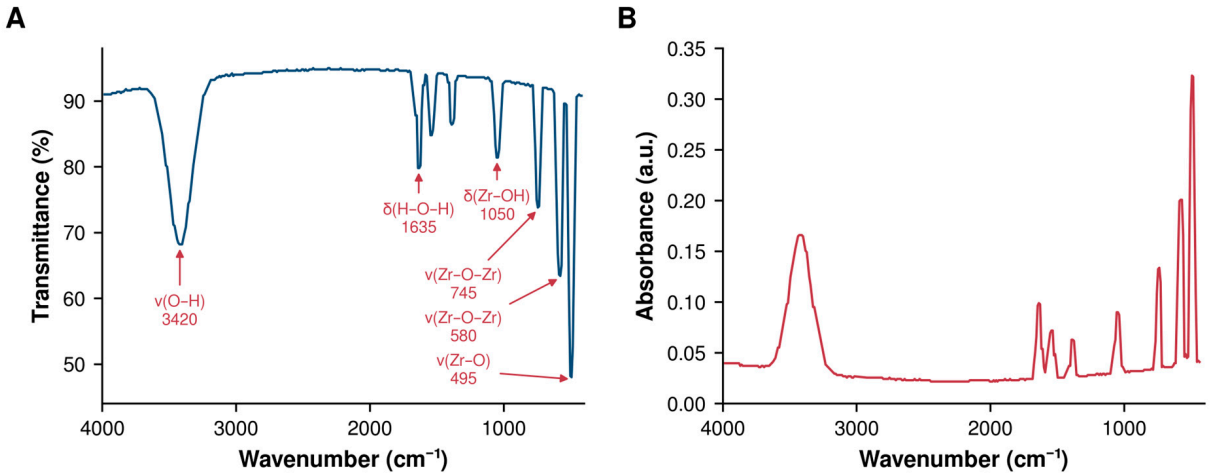


Figure 4. FTIR spectra of ZrO_2 NPs in transmittance (**A**) and absorbance (**B**) modes with band assignments.

3.2.4. Optical Properties

The UV–Vis absorption spectrum of the synthesized nanoparticles exhibited a characteristic absorption maximum at 218 nm, with an absorption edge near 235 nm (Supplementary Figure S1). The transmittance spectrum demonstrated high transparency throughout the visible region, indicating minimal optical absorption above 400 nm. Analysis of the corresponding Tauc plot revealed a direct optical band gap of 4.98 eV, confirming the wide-band-gap semiconducting nature of the biosynthesized ZrO_2 NPs.

3.2.5. Hydrodynamic Size and Colloidal Stability

DLS analysis demonstrated a Z-average hydrodynamic diameter of 89.3 ± 1.3 nm with a polydispersity index (PDI) of 0.218 ± 0.008, indicating a moderately monodisperse nanoparticle suspension (Supplementary Figure S2). The intensity-weighted distribution showed a dominant peak at approximately 85 nm and a minor population near 450 nm, likely corresponding to a small fraction of aggregates. The hydrodynamic diameter was greater than the particle size determined by TEM owing to the hydration layer and possible surface-associated organic species surrounding the nanoparticles. Zeta potential analysis showed an average surface charge of −28.5 ± 5.2 mV, indicating moderate colloidal stability and suggesting that electrostatic repulsion contributed to preventing extensive nanoparticle aggregation in deionized water. Because the biological assays were performed in Mueller–Hinton broth, the ionic strength and proteins of the medium are expected to screen the surface charge and may promote aggregation, so the effective particle size under assay conditions may exceed the hydrodynamic diameter reported here.

3.2.6. Elemental Composition

The elemental composition of the synthesized nanoparticles was confirmed by EDX spectroscopy (Supplementary Figure S3). Strong zirconium and oxygen signals were detected, with quantitative analysis revealing 74.12 wt% Zr, 23.45 wt% O, and only 2.43 wt% C. The carbon signal is attributed mainly to the carbon adhesive tape and the ~10 nm carbon coating applied for conductivity, with a possible contribution from adventitious surface contamination, and is therefore not taken as evidence of residual phytochemicals. The measured elemental composition closely approached the theoretical stoichiometry of ZrO_2, and no additional elements were detected. Zirconium was identified by its L- and K-lines (Supplementary Figure S3).

3.2.7. Thermal Stability

Thermogravimetric analysis demonstrated excellent thermal stability of the synthesized nanoparticles (Supplementary Figure S4). The total weight loss from room temperature to 900 °C was approximately 11.5%, occurring in three distinct stages. The first stage (25–200 °C) corresponded to evaporation of physically adsorbed moisture (3.2% weight loss), whereas the second stage (200–420 °C; 5.8% weight loss) represented weight loss that, because the sample had been calcined at 500 °C for 4 h, is more plausibly attributable to dehydroxylation and decomposition of surface carbonate species (see FTIR) than to intact plant-derived organics, although a minor contribution from residual organic species cannot be excluded without comparison with the uncalcined material. A final weight loss of approximately 2.5% occurred between 420 and 600 °C, which may correspond to dehydroxylation, carbonate decomposition, and/or removal of thermally stable organic residues. Above 600 °C, the thermogram reached a stable plateau with a residual mass of approximately 88.5%, confirming the excellent thermal stability and predominantly inorganic nature of the biosynthesized ZrO_2 NPs.

3.3. Potentiation of Rifampicin Activity by Biosynthesized ZrO_2 NPs Against MDR Klebsiella pneumoniae

The antibacterial activity of biosynthesized ZrO_2 NPs, rifampicin, and their combination against the selected MDR *K. pneumoniae* isolate (PX285917) was initially evaluated using the agar well diffusion assay (Figure 5). Biosynthesized ZrO_2 NPs exhibited concentration-dependent antibacterial activity, with inhibition zones increasing progressively as nanoparticle concentration increased. For reference, rifampicin produced a 25 mm zone against isolate PX285917 in the disc-diffusion panel (30 µg disc, Section 3.1), and its MIC was 64 µg/mL by broth microdilution. These measurements are reported as observed values and are not used to assign a formal rifampicin susceptibility category. In contrast, the combined treatment of ZrO_2 NPs and rifampicin produced the largest inhibition zone (29.5 ± 0.7 mm), which was significantly greater than that produced by either treatment alone ($p < 0.05$), indicating enhanced antibacterial efficacy.

To further quantify the antibacterial activity, the MIC and MBC of each agent were determined for all three clinical isolates (Table 1). Against isolate PX285917, biosynthesized ZrO_2 NPs exhibited an MIC of 128 µg/mL and an MBC of 256 µg/mL, whereas rifampicin showed an MIC of 64 µg/mL and an MBC of 128 µg/mL. The two more susceptible isolates gave lower values: PX285918 (ZrO_2 NPs, MIC 64 µg/mL, MBC 128 µg/mL; rifampicin, MIC 32 µg/mL, MBC 64 µg/mL) and PX285919 (ZrO_2 NPs, MIC 128 µg/mL, MBC 256 µg/mL; rifampicin, MIC 16 µg/mL, MBC 64 µg/mL). Replicate determinations differed by at most one twofold dilution, which is within the accepted variability of the broth microdilution method. MBC/MIC ratios were 2 for all agent–isolate combinations except rifampicin against PX285919, for which the ratio was 4; all values are consistent with bactericidal activity (MBC/MIC ≤ 4) [48].

The interaction between biosynthesized ZrO_2 NPs and rifampicin was subsequently evaluated using the checkerboard microdilution assay against all three isolates (Table 2). In isolate PX285917, the combination reduced the MIC of ZrO_2 NPs from 128 to 32 µg/mL and that of rifampicin from 64 to 8 µg/mL. Comparable reductions were obtained in the two more susceptible isolates: in PX285918 the MICs fell from 64 to 16 µg/mL (ZrO_2 NPs) and from 32 to 4 µg/mL (rifampicin), and in PX285919 from 128 to 16 µg/mL and from 16 to 4 µg/mL, respectively. The calculated fractional inhibitory concentration index was 0.375 in all three isolates, indicating a synergistic interaction according to established interpretative criteria. Because biofilm formation is a major determinant of persistent *K. pneumoniae*

infections, the effect of ZrO_2 NPs, rifampicin, and their combination on biofilm formation was subsequently evaluated.

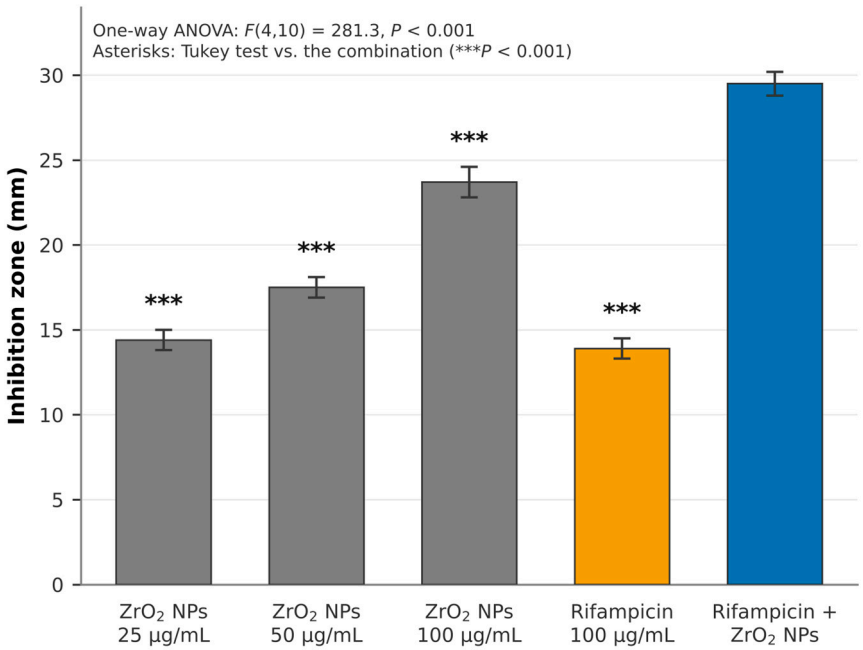


Figure 5. Antibacterial activity of biosynthesized ZrO_2 NPs, rifampicin, and their combination against MDR *Klebsiella pneumoniae* PX285917 determined by the agar well diffusion assay. ZrO_2 NPs were tested at 25, 50 and 100 µg/mL, rifampicin at 100 µg/mL, and the combination at rifampicin 100 µg/mL plus ZrO_2 NPs 100 µg/mL; each well received a total volume of 100 µL. Data are mean ± SD of three independent experiments. Groups were compared by one-way ANOVA ($F(4,10) = 281.3$, $p < 0.001$) followed by Tukey's post hoc test; asterisks denote the comparison of each treatment with the combination (*** $p < 0.001$). All pairwise comparisons are given in Supplementary Table S6.

Table 1. Minimum inhibitory concentration (MIC) and minimum bactericidal concentration (MBC) of biosynthesized ZrO_2 NPs and rifampicin against the three clinical *Klebsiella pneumoniae* isolates. Values are the modal result of three independent experiments; the range is given in parentheses where replicates differed by one twofold dilution.

Isolate	Agent	MIC (µg/mL)	MBC (µg/mL)	MBC/MIC Ratio	Interpretation
PX285917	ZrO_2 NPs	128	256	2	Bactericidal
PX285917	Rifampicin	64	128	2	Bactericidal
PX285918	ZrO_2 NPs	64 (64–128)	128 (128–256)	2	Bactericidal
PX285918	Rifampicin	32 (32–64)	64 (64–128)	2	Bactericidal
PX285919	ZrO_2 NPs	128 (64–128)	256 (128–256)	2	Bactericidal
PX285919	Rifampicin	16 (16–32)	64 (32–64)	4	Bactericidal

Table 2. Checkerboard analysis of the interaction between biosynthesized ZrO_2 NPs and rifampicin against the three clinical *Klebsiella pneumoniae* isolates (three independent experiments per isolate). FICI ≤ 0.5 indicates synergy.

Isolate	MIC ZrO_2 Alone	MIC ZrO_2 in Combination	FIC ZrO_2	MIC RIF Alone	MIC RIF in Combination	FIC RIF	FICI	Interaction
PX285917	128	32	0.250	64	8	0.125	0.375	Synergy
PX285918	64	16	0.250	32	4	0.125	0.375	Synergy
PX285919	128	16	0.125	16	4	0.250	0.375	Synergy

Abbreviations: MIC, minimum inhibitory concentration; RIF, rifampicin; FIC, fractional inhibitory concentration; FICI, fractional inhibitory concentration index. FICI ≤ 0.5, synergy; 0.5 < FICI ≤ 1.0, additive; 1.0 < FICI ≤ 4.0, indifference; FICI > 4.0, antagonism. All MIC values are in µg/mL.

To determine whether the observed activity could be attributed to the plant extract, to residual precursor, or to ZrO_2 as such, three control materials were tested against isolate PX285917 under identical conditions. The *S. officinalis* aqueous extract produced no detectable inhibition at the highest concentration tested (MIC > 16 mg/mL in all three experiments). The zirconium precursor $ZrOCl_2 \cdot 8H_2O$ was weakly active, with a modal MIC of 512 µg/mL (range 512–1024), and commercially available chemically synthesized ZrO_2 gave a modal MIC of 512 µg/mL (range 256–512). Biosynthesized ZrO_2 NPs (MIC 128 µg/mL) were therefore fourfold more active than both the precursor and the chemically synthesized material. The absence of activity of the extract and the low activity of the precursor exclude these as the source of the antibacterial effect observed here, while the difference between the biosynthesized and the chemically synthesized oxide, which amounted to two twofold dilutions, is larger than the variability of the broth microdilution method.

3.4. Time–Kill Kinetics of the ZrO_2 Nanoparticle–Rifampicin Combination

The kinetics of killing were examined over 24 h against *K. pneumoniae* PX285917 at the combination concentrations identified in the checkerboard assay (Figure 6, Table 3). The untreated control grew from 5.70 ± 0.02 to 9.01 ± 0.04 $\log_{10}$ CFU/mL over 24 h. All three treatments produced an initial decline in viable counts, reaching a nadir at 4 h for ZrO_2 NPs (5.20 ± 0.03 $\log_{10}$ CFU/mL) and for rifampicin (4.95 ± 0.03 $\log_{10}$ CFU/mL) and at 8 h for the combination (4.38 ± 0.03 $\log_{10}$ CFU/mL), followed by regrowth by 24 h in every treated arm.

Table 3. Time–kill kinetics of biosynthesized ZrO_2 NPs, rifampicin and their combination against MDR *Klebsiella pneumoniae* PX285917. Values are mean ± standard deviation of three independent biological replicates, expressed as $\log_{10}$ CFU/mL. The 0 h count was determined once from the standardized inoculum used to seed all four arms of the experiment.

Time (h)	Growth Control	ZrO_2 NPs (32 µg/mL)	Rifampicin (8 µg/mL)	ZrO_2 NPs + Rifampicin (32 + 8 µg/mL)
0	5.70 ± 0.02	5.70 ± 0.02	5.70 ± 0.02	5.70 ± 0.02
2	6.33 ± 0.04	5.45 ± 0.03	5.25 ± 0.03	5.05 ± 0.03
4	7.08 ± 0.04	5.20 ± 0.03	4.95 ± 0.03	4.65 ± 0.03
6	7.88 ± 0.04	5.32 ± 0.03	5.12 ± 0.02	4.40 ± 0.03
8	8.54 ± 0.04	5.66 ± 0.04	5.52 ± 0.03	4.38 ± 0.03
24	9.01 ± 0.04	7.11 ± 0.07	6.97 ± 0.08	6.31 ± 0.07

From 2 h onwards the combination was more active than either agent alone at every sampling point, and the difference from rifampicin, the more active of the two single agents, was statistically significant at each of these points ($p < 0.001$). Relative to the untreated control, the combination produced reductions of 3.48 and 4.16 $\log_{10}$ CFU/mL at 6 and 8 h respectively and 2.70 $\log_{10}$ CFU/mL at 24 h, compared with 2.04 $\log_{10}$ CFU/mL for rifampicin alone and 1.90 $\log_{10}$ CFU/mL for ZrO_2 NPs alone at 24 h.

Assessed against the formal time–kill criteria, however, the interaction did not satisfy the definition of synergy. The maximum advantage of the combination over the most active single agent was 1.14 $\log_{10}$ CFU/mL at 8 h and 0.66 $\log_{10}$ CFU/mL at 24 h, both below the ≥2 $\log_{10}$ threshold. None of the treatments was bactericidal: the largest reduction relative to the starting inoculum was 1.32 $\log_{10}$ CFU/mL, recorded for the combination at 8 h. Under these conditions the time–kill data therefore demonstrate a reproducible and statistically significant enhancement of rifampicin activity by the biosynthesized nanoparticles, rather than synergy as defined by the ≥2 $\log_{10}$ criterion.

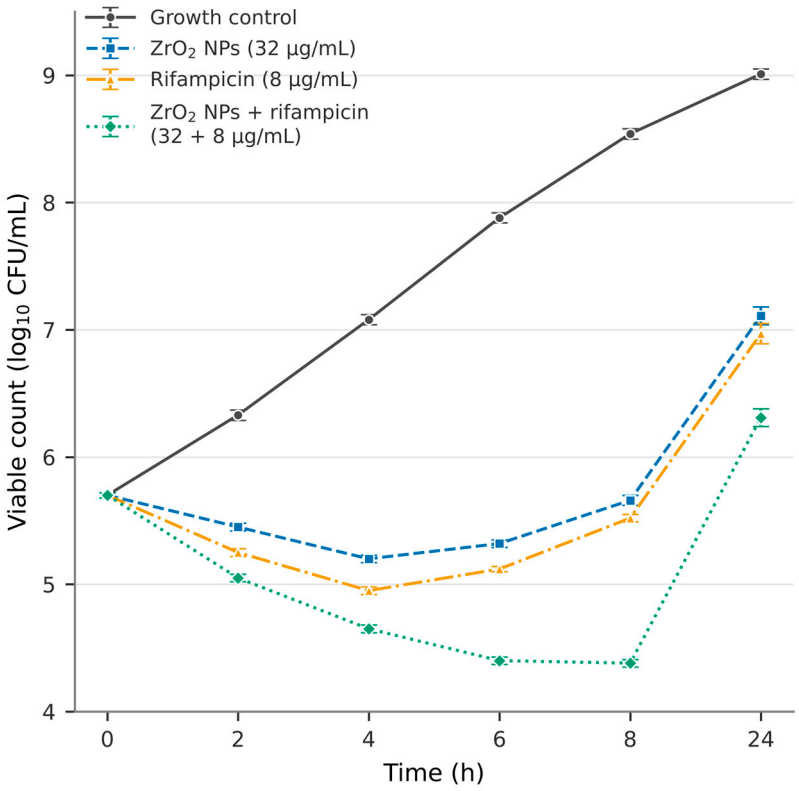


Figure 6. Time–kill kinetics of biosynthesized ZrO_2 NPs, rifampicin and their combination against MDR *Klebsiella pneumoniae* PX285917. Cultures were exposed to ZrO_2 NPs (32 µg/mL), rifampicin (8 µg/mL) or the two agents in combination (32 + 8 µg/mL), and viable counts were determined at 0, 2, 4, 6, 8 and 24 h; an untreated growth control was included. Points are the mean of three independent biological replicates and error bars are the standard deviation; symbol size has been reduced and caps added so that the error bars are legible at every time point. Each series carries its own line style so that the figure remains readable in greyscale. Sampling times are plotted at equal spacing rather than on a linear time scale.

3.5. Antibiofilm Activity of Biosynthesized ZrO_2 NPs and Rifampicin

The antibiofilm activities of biosynthesized ZrO_2 NPs, rifampicin, and their combination against the MDR *K. pneumoniae* isolate PX285917 were evaluated using the crystal violet microtiter plate assay. As presented in Table 4, ZrO_2 NPs alone inhibited biofilm formation by 85.40%, whereas rifampicin alone achieved 82.18% inhibition (mean ± SD of three replicates; one-way ANOVA with Tukey's test, $p < 0.001$ for all pairwise comparisons). Notably, the combination of biosynthesized ZrO_2 NPs and rifampicin produced the greatest inhibition of biofilm formation, 92.59%, despite containing lower concentrations of both agents than the single-agent arms. These findings demonstrate that while both ZrO_2 NPs and rifampicin effectively suppressed biofilm development individually, their combination produced the highest inhibitory effect under the experimental conditions.

To determine whether the antibiofilm effect depended on growth inhibition, the assay was repeated at sub-MIC concentrations (ZrO_2 NPs, 64 µg/mL; rifampicin, 32 µg/mL). Under these conditions, ZrO_2 NPs alone, rifampicin alone, and their combination inhibited biofilm formation by 40.2%, 33.6%, and 45.0%, respectively, showing that biofilm biomass was reduced at concentrations below the planktonic MIC. The combination was only slightly more effective than ZrO_2 NPs alone at these concentrations, so a synergistic antibiofilm effect is not claimed at sub-MIC levels. Viable counts of biofilm cells recovered under the same conditions were 1.0×10^8 CFU/mL (untreated), 8.8×10^7 (ZrO_2 NPs), 8.1×10^7 (rifampicin), and 7.54×10^7 CFU/mL (combination), corresponding to reductions of 12.0%,

19.0%, and 24.6% (less than 0.15 $\log_{10}$). These reductions in viability were much smaller than the reductions in crystal-violet biomass, indicating that the decrease in biomass at sub-MIC concentrations was not accompanied by a comparable loss of viable cells. The sub-MIC experiment was performed separately from the main assay, as an independent experiment using a higher initial inoculum density than in the main assay. Because a higher inoculum is expected to reduce the apparent activity of antimicrobial agents (inoculum effect), the inhibition values obtained in the two experiments are not directly comparable, and the sub-MIC data are presented only to show that biofilm biomass was reduced at concentrations below the planktonic MIC.

Table 4. Effect of biosynthesized ZrO_2 NPs, rifampicin and their combination on biofilm of MDR *Klebsiella pneumoniae* PX285917, measured by the crystal violet microtiter plate assay in three separate experiments: inhibition of biofilm formation at inhibitory concentrations, inhibition of biofilm formation at sub-inhibitory concentrations (performed with an initial inoculum of 1×10^7 CFU/mL), and reduction of preformed biofilm. Values are mean ± SD of three independent experiments; where no SD is given the value is the mean of three replicates. Because the three experiments used different inocula and exposure schedules, the percentages are not directly comparable between blocks.

Assay	Treatment	Concentration (μg/mL)	Reduction in Biofilm Biomass (%)
Inhibition of biofilm formation (treatments present from inoculation)	ZrO_2 NPs	150	85.40 ± 0.03
	Rifampicin	64	82.18 ± 0.43
	ZrO_2 NPs + rifampicin	32 + 8	92.59 ± 0.21
Inhibition of biofilm formation at sub-inhibitory concentrations	ZrO_2 NPs	64	40.2
	Rifampicin	32	33.6
	ZrO_2 NPs + rifampicin	64 + 32	45.0
Preformed biofilm (formed 24 h, then treated 24 h)	ZrO_2 NPs	32	27.0
	Rifampicin	8	9.0
	ZrO_2 NPs + rifampicin	32 + 8	45.0

Activity against established biofilms was assessed in a separate experiment in which biofilms were allowed to form for 24 h before treatment. After a further 24 h of exposure, crystal violet staining gave optical densities of 1.00 ± 0.04 (untreated), 0.91 ± 0.03 (rifampicin, 8 μg/mL), 0.73 ± 0.03 (ZrO_2 NPs, 32 μg/mL) and 0.55 ± 0.04 (combination, 32 + 8 μg/mL), corresponding to reductions in biomass of 9.0%, 27.0% and 45.0%, respectively. Preformed biofilms were therefore considerably less susceptible than biofilm formation, which was reduced by 82–93% when the treatments were present from the time of inoculation; this difference is consistent with the greater tolerance of mature biofilms and indicates that the high inhibition percentages recorded in the formation assay should not be taken as a measure of activity against established biofilms. To determine whether the observed phenotypic effects were associated with modulation of bacterial resistance mechanisms, the expression of key resistance-associated genes was subsequently analyzed by RT-qPCR.

3.6. Indirect Assessment of EtBr Accumulation and Retention

To investigate whether the enhanced activity of rifampicin in combination with ZrO_2 NPs was associated with altered accumulation of a fluorescent efflux substrate, an indirect EtBr retention assay was performed. EtBr fluorescence was monitored over 15 min, with

higher fluorescence retention indicating greater intracellular retention of the fluorescent probe, which was interpreted as reduced extrusion of the probe.

As shown in Table 5 and Supplementary Figure S6, fluorescence was recorded every 2.5 min over 15 min. The no-cell blanks remained flat over this period and did not differ from the buffer-plus-EtBr blank, excluding optical interference by the nanoparticles, and viable counts under the assay conditions remained within 7.2% of the untreated control (Supplementary Table S4).

Table 5. Time course of intracellular EtBr retention (relative fluorescence, %) in MDR *Klebsiella pneumoniae* PX285917. Values are the mean ± SD of three independent experiments. CCCP, carbonyl cyanide m-chlorophenylhydrazone.

Treatment	Concentration	0 min	2.5 min	5 min	7.5 min	10 min	12.5 min	15 min
Untreated control	—	95.0 ± 2.3	84.2 ± 2.5	73.5 ± 2.1	63.8 ± 2.4	54.7 ± 1.9	46.2 ± 2.0	39.0 ± 1.5
Rifampicin	8 µg/mL	95.7 ± 2.5	87.4 ± 2.3	78.5 ± 2.4	68.9 ± 2.0	59.8 ± 2.1	51.2 ± 1.8	44.3 ± 1.5
ZrO_2 NPs	32 µg/mL	96.3 ± 2.4	91.8 ± 2.2	85.6 ± 2.5	79.3 ± 2.1	72.5 ± 2.3	66.4 ± 2.0	61.4 ± 1.7
ZrO_2 NPs + rifampicin	32 + 8 µg/mL	96.8 ± 2.4	93.1 ± 2.3	88.7 ± 2.1	83.9 ± 2.4	78.8 ± 2.0	74.1 ± 2.2	70.4 ± 1.9
CCCP	50 µM	96.0 ± 1.2	94.5 ± 1.3	89.4 ± 1.4	83.5 ± 1.5	78.2 ± 1.4	72.5 ± 1.6	69.8 ± 1.5
CCCP + ZrO_2 NPs	50 µM + 32 µg/mL	96.5 ± 1.4	94.8 ± 1.5	92.5 ± 1.6	90.2 ± 1.7	88.0 ± 1.8	85.8 ± 1.7	83.5 ± 1.9

A distinction should be drawn between accumulation and retention. Accumulation is the net entry of the probe during the loading phase, which a compromised envelope increases; retention is the fraction of the accumulated probe that remains intracellular once efflux is energized, which inhibition of efflux increases. Greater permeability therefore raises the amount of probe present at the start of the energized phase, whereas the rate at which fluorescence then decays reflects extrusion. The present assay does not fully separate the two, which is why the propidium iodide measurements and the CCCP comparator were included. With that qualification, the data indicate that ZrO_2 NPs, particularly when combined with rifampicin, increased EtBr retention in *K. pneumoniae* cells, consistent with reduced probe efflux; because EtBr is a substrate of several efflux systems, increased retention may also reflect membrane damage or loss of proton motive force.

To determine whether this retention could be explained by loss of membrane integrity rather than by reduced efflux, propidium iodide (PI) uptake was measured under the same conditions. Relative to fully permeabilized cells (100%), PI signals were 10.0 ± 0.4% in untreated cells, 15.0 ± 0.8% after rifampicin, 25.0 ± 1.3% after ZrO_2 NPs, 35.0 ± 1.7% after the combination and 20.0 ± 1.3% after CCCP. ZrO_2 NPs therefore caused a measurable increase in membrane permeability, and the combination produced the largest increase of all treatments tested. The greater EtBr retention observed with ZrO_2 NPs cannot therefore be attributed to inhibition of efflux alone, because a compromised envelope may also allow increased entry of the probe. CCCP achieved a retention comparable to that of the combination (69.8% versus 70.4% at 15 min) while increasing PI uptake much less (20.0% versus 35.0%), indicating that the retention seen with the nanoparticle combination is accompanied by considerably more membrane permeabilization than that produced by a classical efflux inhibitor. That retention increased further when ZrO_2 NPs were added to CCCP also suggests that the nanoparticles act, at least in part, through a mechanism additional to dissipation of the proton-motive force.

3.7. Effect of Biosynthesized ZrO_2 NPs Combined with Rifampicin on the Expression of Antibiotic Resistance-Associated Genes in MDR Klebsiella pneumoniae

The relative expression of the resistance-associated genes *acrAB*, *ompK35*, and *ompK36* was quantified by RT-qPCR following treatment with the ZrO_2 nanoparticle–rifampicin combination (Table 6 and Figure 7).

Table 6. Relative expression of *acrAB*, *ompK35* and *ompK36* in MDR *Klebsiella pneumoniae* PX285917 after treatment with biosynthesized ZrO_2 NPs alone, rifampicin alone, and their combination, each compared with the same untreated control. Values are the mean ± SD of three independent biological replicates, each run in technical triplicate. ↓, downregulation relative to the untreated control, given as the percentage reduction in relative expression; "No change", relative expression not significantly different from the control.

Treatment	Gene	Ct Control (Mean ± SD)	Ct Treated (Mean ± SD)	Relative Expression $2^{-\Delta\Delta Ct}$ (Mean ± SD)	Change
ZrO_2 NPs (32 µg/mL)	16S–23S rRNA ITS (reference)	20.16 ± 0.06	20.10 ± 0.10	—	Reference
ZrO_2 NPs (32 µg/mL)	*acrAB*	20.36 ± 0.05	22.22 ± 0.13	0.265 ± 0.005	↓ 73.5%
ZrO_2 NPs (32 µg/mL)	*ompK35*	23.51 ± 0.19	23.42 ± 0.13	1.024 ± 0.020	No change
ZrO_2 NPs (32 µg/mL)	*ompK36*	22.26 ± 0.13	22.32 ± 0.13	0.922 ± 0.018	No change
Rifampicin (8 µg/mL)	16S–23S rRNA ITS (reference)	20.16 ± 0.06	20.10 ± 0.05	—	Reference
Rifampicin (8 µg/mL)	*acrAB*	20.36 ± 0.05	22.13 ± 0.08	0.281 ± 0.025	↓ 71.9%
Rifampicin (8 µg/mL)	*ompK35*	23.51 ± 0.19	23.27 ± 0.08	1.138 ± 0.098	No change
Rifampicin (8 µg/mL)	*ompK36*	22.26 ± 0.13	22.17 ± 0.08	1.026 ± 0.089	No change
Combination (32 + 8 µg/mL)	16S–23S rRNA ITS (reference)	20.16 ± 0.06	20.32 ± 0.03	—	Reference
Combination (32 + 8 µg/mL)	*acrAB*	20.36 ± 0.05	23.94 ± 0.13	0.094 ± 0.007	↓ 90.6%
Combination (32 + 8 µg/mL)	*ompK35*	23.51 ± 0.19	25.89 ± 0.15	0.215 ± 0.018	↓ 78.5%
Combination (32 + 8 µg/mL)	*ompK36*	22.26 ± 0.13	24.08 ± 0.12	0.318 ± 0.019	↓ 68.2%

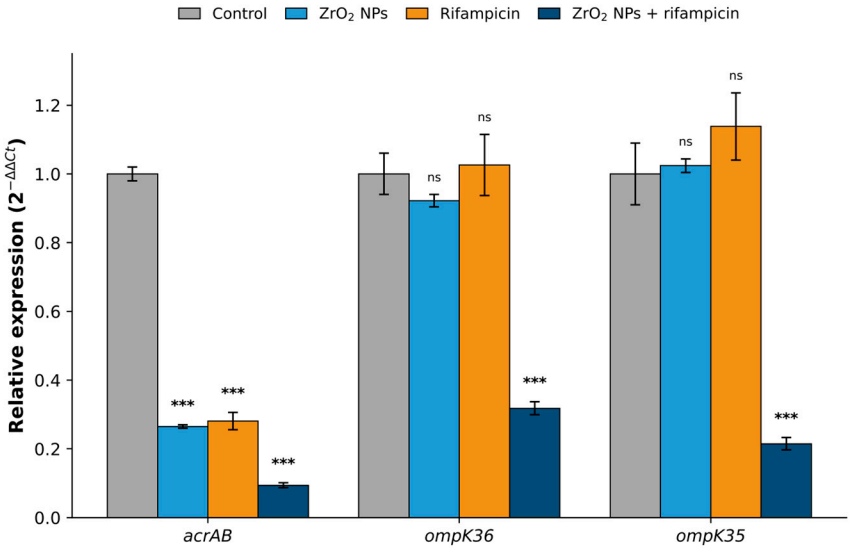


Figure 7. Relative expression of *acrAB*, *ompK35* and *ompK36* in MDR *Klebsiella pneumoniae* PX285917 after treatment with biosynthesized ZrO_2 NPs alone (32 µg/mL), rifampicin alone (8 µg/mL), or their combination (32 + 8 µg/mL) for 24 h, each compared with the same untreated control. Expression was normalized to the 16S–23S rRNA ITS reference gene and calculated using the $2^{-\Delta\Delta Ct}$ method. Data are mean ± SD of three independent biological replicates, each run in technical triplicate. Each treatment was compared with the control for each gene on ΔCt values (Welch's *t*-test); *** $p < 0.001$; ns, not significant.

The combined treatment with biosynthesized ZrO_2 NPs and rifampicin significantly suppressed the expression of all examined genes compared with the untreated control (mean ± SD, n = 3; $p < 0.001$ for each gene). Among the investigated genes, *acrAB* exhibited the greatest reduction in expression, with a relative fold change of 0.094 ± 0.007, corresponding to approximately 90.6% downregulation. Similarly, *ompK35* expression decreased to 0.215 ± 0.018-fold, representing a 78.5% reduction, whereas *ompK36* showed a relative expression level of 0.318 ± 0.019, corresponding to approximately 68.2% downregulation (Table 6). These values reflect transcript levels only; because permeability was not measured, the *ompK35* and *ompK36* changes are interpreted as envelope stress or porin remodeling rather than altered outer-membrane permeability.

As shown in Figure 7 and Table 6, the combination reduced the relative expression of *acrAB*, *ompK35* and *ompK36* compared with untreated cells ($p < 0.001$). The single-agent arms showed that ZrO_2 NPs and rifampicin each reduced *acrAB* expression to a similar extent when applied alone (relative expression 0.265 ± 0.005 and 0.281 ± 0.025, respectively), whereas the combination produced a larger reduction (0.094 ± 0.007). By contrast, neither agent alone altered the expression of the porin genes *ompK35* (1.024 ± 0.020 and 1.138 ± 0.098) or *ompK36* (0.922 ± 0.018 and 1.026 ± 0.089), which were reduced only after combined treatment. The Ct values of the 16S–23S rRNA ITS reference gene varied by 0.22 cycles across all four conditions (20.10–20.32), indicating that its expression was not appreciably affected by the treatments.

Because the ITS reference gene was stable across all conditions and single-agent arms were included, the transcriptional changes can be attributed to the treatments rather than to the normalization. Both agents alone reduced *acrAB* expression, and the combination reduced it further, whereas the porin genes changed only after combined treatment. These measurements were nevertheless made after 24 h at growth-inhibitory concentrations, so a contribution of general growth inhibition or stress cannot be excluded, and transcript abundance does not necessarily reflect protein levels or transporter activity.

3.8. Ultrastructural Alterations in MDR Klebsiella pneumoniae Following Treatment with Biosynthesized ZrO_2 NPs and Rifampicin

Scanning electron microscopy (SEM) was performed to investigate the morphological changes induced by biosynthesized ZrO_2 NPs, rifampicin, and their combination in MDR *K. pneumoniae* (Figure 8). Untreated bacterial cells exhibited the typical short rod (coccobacillary) morphology with smooth, intact cell surfaces and well-defined cellular boundaries, indicating normal structural integrity (Figure 8A).

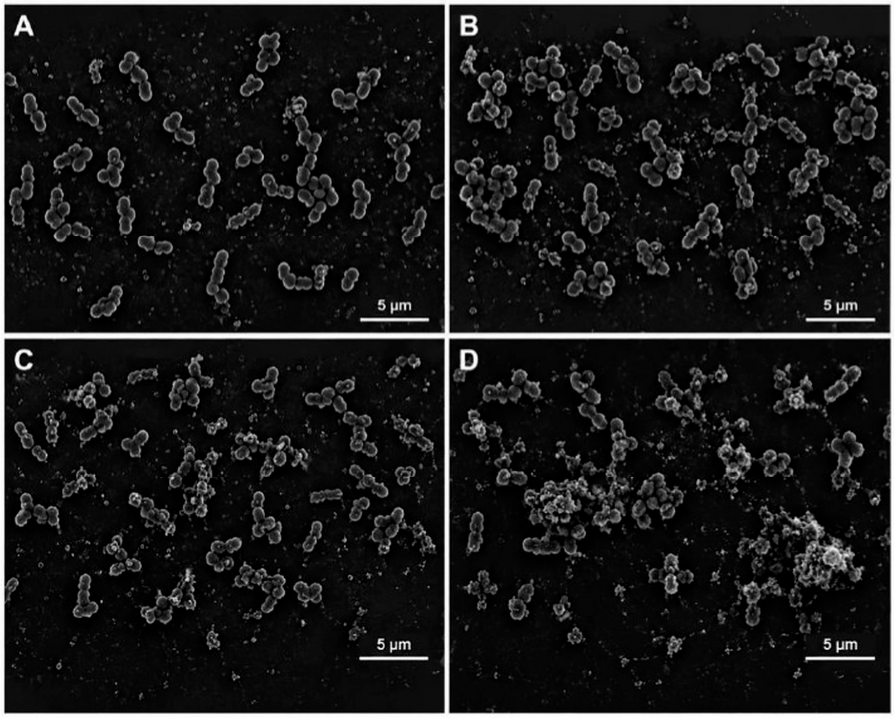


Figure 8. Scanning electron micrographs of MDR *Klebsiella pneumoniae* following different treatments: (**A**) untreated control; (**B**) rifampicin-treated cells; (**C**) ZrO_2 nanoparticle-treated cells; and (**D**) combination-treated cells. Progressive ultrastructural damage, including membrane disruption, surface roughening, cellular shrinkage, and loss of integrity, was most pronounced following combination treatment.

Treatment with rifampicin alone produced moderate morphological alterations characterized by slight surface irregularities and partial deformation of bacterial cells (Figure 8B). Similarly, exposure to biosynthesized ZrO_2 NPs resulted in noticeable structural damage, including surface roughening, membrane distortion, and localized cell shrinkage, indicating that the nanoparticles possessed intrinsic antibacterial activity (Figure 8C).

The most pronounced ultrastructural alterations were observed following the combined treatment with biosynthesized ZrO_2 NPs and rifampicin (Figure 8D). Bacterial cells exhibited extensive membrane disruption, severe surface collapse, deformation of the normal cell shape, and leakage of intracellular contents. Several cells appeared completely lysed, with a marked loss of cellular integrity compared with both the untreated control and the individual treatments.

4. Discussion

This study set out to establish whether biosynthesized ZrO_2 NPs can restore the activity of an antibiotic that the Gram-negative envelope ordinarily excludes. Three findings emerge. First, the nanoparticles lowered the concentration of rifampicin required to inhibit MDR *K. pneumoniae* to an extent that met the checkerboard criterion for synergy, and did so reproducibly in three clinical isolates of differing baseline susceptibility. Second, the control experiments place that activity with the biosynthesized material itself rather than with residual plant extract, the zirconium precursor, or ZrO_2 as such. Third, the mechanistic experiments indicate that two processes contribute—increased permeability of the cell envelope and reduced expression of the principal efflux determinant of this species—and that neither alone accounts for the result. If these observations hold in vivo, the practical interest lies less in the nanoparticles as antibacterial agents than in their capacity to return an existing, well-characterised and inexpensive drug to a pathogen from which it is currently excluded. The sections below consider each line of evidence and its limitations in turn.

4.1. MDR Phenotype and Selection of the Representative Isolate

The rapid emergence and global dissemination of MDR *K. pneumoniae* have become a major public health concern, substantially limiting the effectiveness of conventional antimicrobial therapy and increasing the incidence of healthcare-associated infections. The remarkable ability of *K. pneumoniae* to acquire multiple resistance determinants through chromosomal mutations, plasmid-mediated gene transfer, and multidrug efflux systems has contributed to the widespread occurrence of strains resistant to β-lactams, fluoroquinolones, aminoglycosides, and other clinically important antibiotics [1–3]. Consequently, the development of alternative antimicrobial strategies capable of restoring antibiotic susceptibility has become an urgent research priority.

Hierarchical clustering of the inhibition zone data separated PX285917 from the other two isolates, which clustered together. PX285917 was non-susceptible across the widest range of antimicrobial categories and was therefore taken as the representative MDR strain; the individual zone diameters are given in the Results and in Supplementary Table S1. Such phenotypic heterogeneity among clinical *K. pneumoniae* isolates is well documented and reflects the continuous evolution of resistance in hospital environments [4–9].

4.2. Green Synthesis and Physicochemical Characteristics of ZrO_2 NPs

Green synthesis has been proposed as an environmentally sustainable approach for producing metal oxide nanoparticles, using plant-derived phytochemicals in place of hazardous reducing agents [24,25,27,28]. In the present study, ZrO_2 NPs were prepared using *S. officinalis* extract followed by calcination at 500 °C. The extract itself was inactive at the highest concentration tested, and the zirconium precursor was only weakly active, so nei-

ther accounts for the antibacterial effect observed here. Biosynthesized ZrO_2 NPs were fourfold more active than commercially available chemically synthesized ZrO_2. Because the commercial material is specified by the supplier only as <100 nm by TEM, and its crystalline phase and specific surface area were not determined here, the two oxides were not matched for the properties that govern antibacterial activity; the difference is therefore consistent with a contribution of the synthesis route, but particle size, phase and surface area cannot be excluded as alternative explanations.

TEM demonstrated that the synthesized nanoparticles were predominantly quasi-spherical with nanoscale dimensions and a relatively narrow size distribution. Dynamic light scattering analysis revealed a larger hydrodynamic diameter than that observed by TEM, which is expected because DLS measures the hydrated particle together with the surrounding solvation layer and possible surface-associated organic species, whereas TEM determines the physical core diameter under dry conditions [49]. Such differences are frequently reported for biosynthesized nanoparticles and reflect the complementary nature of the two analytical techniques rather than inconsistency in particle characterization.

X-ray diffraction indicated monoclinic ZrO_2 with no detectable secondary crystalline phases, and EDX showed zirconium and oxygen as the main elements, with a minor carbon signal attributable mainly to the carbon tape and coating.

FTIR spectra showed Zr–O lattice vibrations together with bands attributable to surface hydroxyl and carbonate species. Because the material was calcined at 500 °C, only minor residual organic species would be expected.

Two limitations of this characterization should be stated plainly. First, the chemical composition of the *S. officinalis* extract was not determined in this study. Plant extracts used for green synthesis owe their reducing and stabilizing capacity to polyphenols, flavonoids and terpenoids [24,25], and *S. officinalis* is a well-characterized source of all three: its extracts are reported to contain the phenolic acids rosmarinic and caffeic acid, the flavonoids luteolin-7-glucoside, quercetin and rutin, and the phenolic diterpenes carnosic acid and carnosol, together with the triterpenoids ursolic and oleanolic acid [50]. Constituents of these classes are therefore the plausible reducing and capping agents in the present preparation. This attribution rests on the published composition of the species and not on any measurement made on the extract used here; profiling it by GC-MS or LC-MS would be required to identify the constituents actually involved. Second, because the product was calcined at 500 °C for 4 h, a treatment expected to remove most adsorbed organic material, the role of the extract can be demonstrated for the synthesis step but not for persistent surface capping of the recovered nanoparticles: the FTIR spectrum of the calcined material shows Zr–O lattice vibrations with surface hydroxyl and carbonate bands but no feature that can be assigned unambiguously to intact phytochemicals, the EDX carbon signal is attributable to the carbon tape and conductive coating, and the weight loss above 200 °C is at least as consistent with dehydroxylation and carbonate decomposition as with organic residues. Establishing whether capping species survive calcination would require FTIR and TGA of the uncalcined precursor alongside the calcined product.

The wide optical band gap and moderate negative zeta potential are consistent with previous reports for ZrO_2 NPs [27,51].

4.3. Antibacterial Activity and Rifampicin Potentiation

Biosynthesized ZrO_2 NPs inhibited the growth of the tested MDR *K. pneumoniae* isolate in a concentration-dependent manner, with an MBC/MIC ratio of 2, consistent with previous reports of antibacterial activity of metal oxide nanoparticles [27,52–55].

Rifampicin alone was considerably less effective than the combination, which is consistent with the intrinsic characteristics of Gram-negative bacteria: the outer membrane

acts as a permeability barrier that limits rifampicin penetration, while overexpression of resistance–nodulation–division efflux pumps and mutations affecting *rpoB* further reduce intracellular concentrations. Because no interpretive breakpoint exists for rifampicin against Enterobacterales, the values reported here are descriptive and are not used to classify the isolate. These limitations are precisely why rifampicin is now investigated as a component of combination therapy rather than as monotherapy.

The principal finding of the present study is the potentiation of rifampicin activity by biosynthesized ZrO_2 NPs, which was reproduced in all three clinical isolates examined and met the checkerboard criterion for synergy in each of them. Synergistic interactions between antibiotics and various metal oxide nanoparticles have been reported previously [10,19,20,27,28,33].

In the checkerboard assay the combination lowered the inhibitory concentration of both agents substantially, and the resulting fractional inhibitory concentration index met the conventional threshold for synergy in every isolate tested. That the same index was obtained in three isolates of differing baseline susceptibility is the more important observation, since it indicates that the interaction does not depend on the starting resistance phenotype. The mechanistic experiments reported below were performed in PX285917 alone.

The checkerboard and time–kill assays did not give entirely concordant results, and this difference merits comment. The checkerboard assay indicated synergy (FICI 0.375), whereas in the time–kill experiment the combination enhanced killing significantly at every sampling point but by less than the 2 $\log_{10}$ margin required for synergy by that method. Divergence between the two approaches is well recognised and reflects the different quantities they measure: the checkerboard evaluates inhibition of visible growth at a single 24 h endpoint across a matrix of concentrations and therefore reports the extent to which the required inhibitory concentration of each agent is lowered, whereas the time–kill assay measures the rate and magnitude of killing at fixed concentrations. An agent may substantially reduce the inhibitory concentration of a partner drug without increasing the extent of killing a hundredfold at a single fixed concentration.

Taken together, the two assays indicate that the biosynthesized ZrO_2 NPs lower the concentration of rifampicin required to inhibit growth and increase the extent of killing achieved at a given concentration, without converting a bacteriostatic exposure into a bactericidal one. The time–kill experiment was performed at the combination concentrations derived from the checkerboard assay, that is, close to the inhibitory concentration of the combination; killing at concentrations near the MIC is characteristically modest, and the regrowth observed in all treated cultures by 24 h indicates that a surviving subpopulation persists under these conditions. Whether greater multiples of the combination concentration would meet the time–kill definition of synergy was not examined here.

Collectively, the microbiological findings indicate that biosynthesized ZrO_2 NPs exhibit direct antibacterial activity and potentiate rifampicin against the three MDR *K. pneumoniae* isolates tested, synergistically by the checkerboard criterion, supporting further investigation of this combination.

4.4. Antibiofilm Activity

Biofilm formation contributes to the persistence of *K. pneumoniae* infections, and the three biofilm experiments reported here measure different things. In the main assay the treatments were present from the moment of inoculation and at or above inhibitory concentrations, so the 82–93% reductions recorded there are to a large extent a consequence of preventing the population from establishing at all rather than evidence of a specific antibiofilm action. The sub-inhibitory experiment separates the two: biomass still fell by a third to a half while viable counts fell by less than 0.15 $\log_{10}$, so at these concentrations

the treatments reduce the amount of matrix and adherent material without killing the cells that produce it. This dissociation between biomass and viability is the more informative result, and it points to interference with attachment and matrix production rather than to a bactericidal mechanism. Preformed biofilms were markedly less susceptible, which is expected: once the matrix is established it limits penetration, and the embedded population is metabolically slower and therefore less vulnerable to an agent whose target is transcription. The practical implication is that the combination is better suited to preventing biofilm establishment, for example on a freshly placed device surface, than to clearing a mature biofilm, and the high percentages obtained in the formation assay should not be read as activity against established biofilm. These observations can be set against the small existing literature on the two components. ZrO_2 NPs have been reported to act on biofilms of Gram-positive organisms, a minimum biofilm eradication concentration ($MBEC_{80}$) of 22.8 µg/mL being reported against both *Streptococcus mutans* and *Enterococcus faecalis* [56], although comparable data for Gram-negative species remain scarce, and the reductions reported here for *K. pneumoniae* therefore extend that observation to an organism in which the envelope itself is the principal obstacle. Rifampicin, for its part, is unusual among antibacterial agents in penetrating the biofilm matrix; because resistance emerges rapidly through *rpoB* mutation, however, it is recommended only in combination, and combination regimens are associated with better outcomes against established biofilm infections [57]. The present results are consistent with both accounts. The combination acted principally on biofilm establishment rather than on the mature structure, which is what the penetration and slow-growth arguments predict, and the dissociation between biomass and viability at sub-inhibitory concentrations points to interference with attachment and matrix production of the kind described for metal oxide nanoparticles rather than to the transcriptional killing by which rifampicin acts. The established requirement that rifampicin be given with a partner agent is also directly relevant to the strategy examined here, since the nanoparticles constitute such a partner and act on a different target.

4.5. Efflux Activity and Resistance-Associated Gene Modulation

Treatment with ZrO_2 NPs, alone or with rifampicin, was associated with greater EtBr retention than in untreated cells. The assay behaved as expected with the efflux inhibitor CCCP, which produced a retention comparable to that of the combination, so the readout does detect inhibition of energy-dependent efflux. The contribution of these barriers in this species is well documented: the AcrAB–TolC pump of the RND family is the principal efflux determinant of *K. pneumoniae* and reduces susceptibility to structurally unrelated agents [6,7,11], while loss or reduced expression of the major porins OmpK35 and OmpK36 lowers outer-membrane permeability and raises resistance to β-lactams and other antibiotics [8,9]. Together these two mechanisms account for much of the intrinsic resistance of the species, and they are the reason that intrinsically potent but poorly permeant agents such as rifampicin are excluded, which is also why outer-membrane permeabilisers have been shown to restore its activity against Gram-negative organisms [15,18]. Two further observations show that more than efflux inhibition is involved. First, the parallel PI measurements show that the nanoparticle treatments increased membrane permeability, and that the combination did so to a greater extent than CCCP; a compromised envelope allows increased entry of the probe as well as reduced extrusion. Second, retention increased further when ZrO_2 NPs were combined with CCCP, which would not be expected if the nanoparticles acted solely by dissipating the proton-motive force. Taken together, the data indicate that reduced efflux and increased membrane permeability both contribute to the observed retention; their relative contributions were not resolved by these experiments.

Direct measurement of intracellular rifampicin accumulation, of membrane potential and of pump-specific activity in defined mutants would quantify each.

Relative expression of *acrAB* was reduced by both agents individually and to a greater extent by the combination, while *ompK35* and *ompK36* were reduced only after combined treatment. The stability of the ITS reference gene across all four conditions (Ct range 0.22 cycles) supports the validity of the normalization. These data should nevertheless be interpreted with caution: the measurements were made after 24 h at growth-inhibitory concentrations, so general growth inhibition or stress may contribute; amplification efficiencies were not determined experimentally; and transcript levels do not necessarily reflect protein abundance or pump activity. Moreover, reduced expression of the porin genes *ompK35* and *ompK36* would be expected to decrease, rather than increase, outer-membrane permeability. Rifampicin is a large, lipophilic molecule that crosses the Gram-negative outer membrane chiefly by partitioning through the lipid bilayer rather than through the water-filled porin channels [12], so reduced porin expression would not in itself be expected to limit its entry. These changes are therefore more readily interpreted as part of a general envelope-stress response than as the route to greater rifampicin uptake, which the PI data instead attribute to increased permeability of the lipid bilayer.

4.6. Ultrastructural Alterations and Membrane Disruption

Untreated cells exhibited the characteristic morphology of healthy *K. pneumoniae*, with intact short rod-shaped (coccobacillary) cells, smooth outer surfaces, and well-defined cellular boundaries, confirming preservation of normal envelope integrity. In contrast, exposure to rifampicin alone induced only moderate morphological alterations, including slight surface irregularities and partial deformation. These findings are consistent with the known mechanism of rifampicin, which primarily inhibits bacterial DNA-dependent RNA polymerase rather than directly targeting the cell envelope. Consequently, the structural alterations observed following rifampicin treatment are likely secondary consequences of impaired transcription, metabolic arrest, and progressive cellular deterioration rather than direct membrane damage [12–14].

Treatment with ZrO_2 NPs alone was associated with surface roughening, cell shrinkage, and distortion of the rod-shaped morphology, changes similar to those reported for other metal oxide nanoparticles [19,20,27,52,58,59].

The most pronounced alterations, including cell deformation and apparent loss of cellular integrity, were observed after combination treatment. SEM provides qualitative evidence; whether the membrane damage precedes or follows growth inhibition was not determined.

4.7. Significance and Future Directions

Rifampicin is among the most potent antibacterial agents available, yet it is of little use against *K. pneumoniae* because the Gram-negative outer membrane excludes it and efflux removes what little enters. Restoring its activity would redeploy a well-characterised and inexpensive drug against a pathogen that the WHO lists as a critical priority, a considerably shorter route than developing a new chemical entity. The results reported here show that biosynthesized ZrO_2 NPs achieve this in vitro, and the interpretation is strengthened by the control set: the plant extract alone, the zirconium precursor and a commercially sourced chemically synthesized oxide were all tested, establishing that the activity belongs to the biosynthesized nanoparticles rather than to residual extract or precursor. The mechanistic experiments likewise included an efflux-inhibitor comparator, a membrane-integrity readout, single-agent arms, and a reference gene that proved stable across all conditions.

Future work should define the mechanism. Because the nanoparticle treatments increased membrane permeability, the EtBr retention data cannot by themselves separate

reduced efflux from increased probe entry; direct measurement of intracellular rifampicin accumulation, of membrane potential and of pump activity in defined mutants would resolve this. The transcriptional changes were measured after 24 h at inhibitory concentrations, and confirmation at earlier time points and at the protein level is warranted. The mechanistic experiments were conducted in PX285917, and extension to genetically diverse isolates, including reference strains and carbapenem-resistant and hypervirulent lineages, will establish how general the effect is. Benchmarking against outer membrane permeabilizers [15] and characterized efflux pump inhibitors [11,60], together with assays targeting envelope biogenesis and the envelope stress response [18], would place the nanoparticles relative to agents with defined mechanisms. Cytotoxicity and haemocompatibility testing is required before any therapeutic application can be considered.

5. Conclusions

Biosynthesized ZrO_2 NPs restored the activity of rifampicin against MDR *K. pneumoniae* in vitro. The interaction met the checkerboard criterion for synergy in all three clinical isolates (FICI 0.375) despite their differing baseline susceptibility, and control experiments with the plant extract, the zirconium precursor and a chemically synthesized oxide place the activity with the biosynthesized material rather than with its components. Mechanistically, the combination both increased membrane permeability and lowered expression of the principal efflux determinant of this species, and the PI and CCCP comparisons indicate that neither effect alone accounts for the result. The study does not establish synergy by the time–kill criterion, does not resolve the relative contribution of permeabilization and efflux inhibition, and rests on mechanistic experiments performed in a single isolate. Direct measurement of intracellular rifampicin accumulation, extension to genetically diverse strains, and cytotoxicity testing are the next steps required before any therapeutic potential can be judged.

Supplementary Materials: The following supporting information can be downloaded at: https://www.mdpi.com/article/10.3390/pathogens15121249/s1, Table S1: Antibiotic disc panel, disc potency, CLSI interpretive criteria and zone diameters with the resulting S/I/R categories for the three clinical *Klebsiella pneumoniae* isolates. Categories were assigned from the measured zone diameters using the breakpoints shown (CLSI M100, 35th edition, 2025); Table S2: Crystallite size of ZrO_2 nanoparticles calculated with the Scherrer equation; Table S3: Primers and validation parameters for RT-qPCR; Table S4: Controls for the ethidium bromide (EtBr) retention assay; Table S5: Individual Ct values of the RT-qPCR biological replicates for the untreated control and the ZrO_2 nanoparticle–rifampicin combination; Table S6: All pairwise comparisons of the agar well diffusion data shown in Figure 5 (one-way ANOVA, $F(4,10) = 281.3$, $p < 0.001$, followed by Tukey's honestly significant difference test; n = 3 independent experiments per group). Figure 5 displays only the comparison of each treatment with the combination; the complete matrix is given here; Figure S1: UV–Vis characterization of ZrO_2 nanoparticles: (A) absorption spectrum, (B) transmittance spectrum, and (C) Tauc plot for direct bandgap determination (direct allowed transition; $(\alpha h\nu)^2$ versus $h\nu$; linear fit over 5.1–5.6 eV; Eg = 4.98 eV); Figure S2: DLS and zeta potential analysis of ZrO_2 nanoparticles: (A) size distribution, (B) autocorrelation function, (C) zeta potential distribution, and (D) replicate measurement summary. Z-average diameter, PDI and zeta potential are mean ± SD of three measurements (n = 3); Figure S3: EDX spectrum of ZrO_2 nanoparticles acquired using EDAX APEX system with element identification labels; Figure S4: TGA and DTG curves of ZrO_2 nanoparticles recorded under nitrogen atmosphere at a heating rate of 10 °C/min showing three distinct weight loss stages; Figure S5: Melting-curve (dissociation) analysis of the RT-qPCR products for *acrAB* (A), *ompK35* (B), *ompK36* (C) and the *K. pneumoniae* 16S–23S rRNA ITS reference (D). A single peak was obtained for each target (Tm ≈ 79.0, 86.2, 80.2 and 79.0 °C, respectively; values read from the dissociation curves), indicating specific amplification. The two curves in each panel are the control and treated samples; Figure S6: Time course of intracellular EtBr fluorescence in MDR *K. pneumoniae* PX285917 after treatment with rifampicin

(8 µg/mL), ZrO_2 nanoparticles (32 µg/mL), their combination, the efflux inhibitor CCCP (50 µM) and CCCP combined with ZrO_2 nanoparticles. Fluorescence was recorded every 2.5 min for 15 min and is expressed as a percentage of each sample's initial value. Values are mean ± SD (n = 3) and are the data of Table 5; Figure S7: Representative RT-qPCR amplification plots of *acrAB* (A), *ompK36* (B) and *ompK35* (C) in untreated control cells (sample C) and cells treated with the ZrO_2 nanoparticle–rifampicin combination (sample T). Fluorescence (dRn) is plotted against cycle number; the horizontal line indicates the threshold. Experiments were performed with three biological replicates, each in technical triplicate.

Author Contributions: Conceptualization, R.A.I. and E.Y.T.E.; methodology, R.A.I. and H.I.A.E.; investigation, R.A.I. and H.I.A.E.; validation, R.A.I.; formal analysis, R.A.I., H.I.A.E., A.M.A. and E.M.; resources, A.M.A. and E.M.; data curation, R.A.I.; visualization, R.A.I.; writing—original draft preparation, R.A.I. and H.I.A.E.; writing—review and editing, H.I.A.E., A.M.A., E.Y.T.E. and E.M.; supervision, R.A.I. and E.Y.T.E.; project administration, R.A.I.; funding acquisition, A.M.A. and E.M. All authors have read and agreed to the published version of the manuscript.

Funding: This research received no external funding. The article processing charge was funded by the Deanship of Graduate Studies and Scientific Research, Qassim University (QU-APC-2026). The funder had no role in the design of the study; in the collection, analyses or interpretation of data; in the writing of the manuscript; or in the decision to publish the results.

Institutional Review Board Statement: Ethical approval was not required for this study. The authors did not collect any specimens and had no contact with patients. The bacterial isolates used in this study were provided by the culture collection of the Department of Microbiology, Faculty of Science, Ain Shams University, Cairo, Egypt, and were received and handled as anonymised bacterial cultures carrying no patient-identifying information. No human participants and no identifiable human data were involved.

Informed Consent Statement: The bacterial isolates used in this study were provided by the culture collection of the Department of Microbiology, Faculty of Science, Ain Shams University, Cairo, Egypt, and were received and handled as anonymised bacterial cultures carrying no patient-identifying information. No human participants and no identifiable human data were involved.

Data Availability Statement: The 16S rRNA gene sequences of the three *Klebsiella pneumoniae* isolates reported in this study have been deposited in the NCBI GenBank database under accession numbers PX285917, PX285918 and PX285919. All other data generated or analysed during this study are included in this published article and its Supplementary Material. Further enquiries can be directed to the corresponding authors.

Acknowledgments: The researchers would like to thank the Deanship of Graduate Studies and Scientific Research at Qassim University for financial support (QU-APC-2026). No Generative AI was used. All data were generated by the authors, who reviewed and verified all content and take full responsibility for the work.

Conflicts of Interest: The authors declare no conflicts of interest. The funder had no role in the design of the study; in the collection, analyses or interpretation of data; in the writing of the manuscript; or in the decision to publish the results.

Abbreviations

The following abbreviations are used in this manuscript:

AMR	antimicrobial resistance
ANOVA	analysis of variance
ATCC	American Type Culture Collection
BLAST	Basic Local Alignment Search Tool
CCCP	carbonyl cyanide m-chlorophenylhydrazone
CFU	colony-forming units
CLSI	Clinical and Laboratory Standards Institute

CTAB	cetyltrimethylammonium bromide
DLS	dynamic light scattering
DMSO	dimethyl sulfoxide
DNA	deoxyribonucleic acid
DTG	derivative thermogravimetry
EDX	energy-dispersive X-ray spectroscopy
EPS	extracellular polymeric substance
EtBr	ethidium bromide
EUCAST	European Committee on Antimicrobial Susceptibility Testing
FE-SEM	field-emission scanning electron microscope
FIC	fractional inhibitory concentration
FICI	fractional inhibitory concentration index
FTIR	Fourier-transform infrared spectroscopy
FWHM	full width at half maximum
GC-MS	gas chromatography–mass spectrometry
ITS	internal transcribed spacer
LC-MS	liquid chromatography–mass spectrometry
MBC	minimum bactericidal concentration
MBEC	minimum biofilm eradication concentration
MDR	multidrug-resistant
MIC	minimum inhibitory concentration
MTP	microtiter plate
NCBI	National Center for Biotechnology Information
NPs	nanoparticles
OD	optical density
OD_{600}	optical density at 600 nm
PBS	phosphate-buffered saline
PCR	polymerase chain reaction
PDI	polydispersity index
PI	propidium iodide
PPB	potassium phosphate buffer
RIF	rifampicin
RNA	ribonucleic acid
RND	resistance–nodulation–division
RT-qPCR	reverse-transcription quantitative real-time PCR
SD	standard deviation
SEM	scanning electron microscopy
TEM	transmission electron microscopy
TGA	thermogravimetric analysis
TSB	tryptic soy broth
UV–Vis	ultraviolet–visible spectroscopy
WHO	World Health Organization
XRD	X-ray diffraction
ZrO_2	zirconium dioxide

References

1. Murray, C.J.L.; Ikuta, K.S.; Sharara, F.; Swetschinski, L.; Aguilar, G.R.; Gray, A.; Han, C.; Bisignano, C.; Rao, P.; Wool, E.; et al. Global burden of bacterial AMR in 2019: A systematic analysis. *Lancet* **2022**, *399*, 629–655. [CrossRef] [PubMed]
2. World Health Organization. *WHO Bacterial Priority Pathogens List 2024: Bacterial Pathogens of Public Health Importance to Guide Research, Development and Strategies to Prevent and Control AMR*; World Health Organization: Geneva, Switzerland, 2024.
3. Wyres, K.L.; Holt, K.E. *Klebsiella pneumoniae* as a key trafficker of drug resistance genes from environmental to clinically important bacteria. *Curr. Opin. Microbiol.* **2018**, *45*, 131–139. [CrossRef] [PubMed]
4. Effah, C.Y.; Sun, T.; Liu, S.; Wu, Y. *Klebsiella pneumoniae*: An increasing threat to public health. *Ann. Clin. Microbiol. Antimicrob.* **2020**, *19*, 1. [CrossRef] [PubMed]
5. Martin, R.M.; Bachman, M.A. Colonization, infection, and the accessory genome of *Klebsiella pneumoniae*. *Front. Cell. Infect. Microbiol.* **2018**, *8*, 4. [CrossRef] [PubMed]
6. Du, D.; Wang-Kan, X.; Neuberger, A.; van Veen, H.W.; Pos, K.M.; Piddock, L.J.V.; Luisi, B.F. Multidrug efflux pumps: Structure, function and regulation. *Nat. Rev. Microbiol.* **2018**, *16*, 523–539. [CrossRef] [PubMed]
7. Hernando-Amado, S.; Blanco, P.; Alcalde-Rico, M.; Corona, F.; Reales-Calderón, J.A.; Sánchez, M.B.; Martínez, J.L. Multidrug efflux pumps as main players in intrinsic and acquired resistance to antimicrobials. *Drug Resist. Updat.* **2016**, *28*, 13–27. [CrossRef] [PubMed]

8. Doménech-Sánchez, A.; Martínez-Martínez, L.; Hernández-Allés, S.; Conejo, M.d.C.; Pascual, A.; Tomás, J.M.; Albertí, S.; Benedí, V.J. Role of *Klebsiella pneumoniae* OmpK35 porin in AMR. *Antimicrob. Agents Chemother.* **2003**, *47*, 3332–3335. [CrossRef] [PubMed]
9. Tsai, Y.-K.; Fung, C.-P.; Lin, J.-C.; Chen, J.-H.; Chang, F.-Y.; Chen, T.-L.; Siu, L.K. *Klebsiella pneumoniae* outer membrane porins OmpK35 and OmpK36 play roles in both AMR and virulence. *Antimicrob. Agents Chemother.* **2011**, *55*, 1485–1493. [CrossRef] [PubMed]
10. Allahverdiyev, A.M.; Kon, K.V.; Abamor, E.S.; Bagirova, M.; Rafailovich, M. Coping with antibiotic resistance: Combining nanoparticles with antibiotics and other antimicrobial agents. *Expert Rev. Anti-Infect. Ther.* **2011**, *9*, 1035–1052. [CrossRef] [PubMed]
11. Zack, K.M.; Sorenson, T.; Joshi, S.G. Types and Mechanisms of Efflux Pump Systems and the Potential of Efflux Pump Inhibitors in the Restoration of Antimicrobial Susceptibility, with a Special Reference to *Acinetobacter baumannii*. *Pathogens* **2024**, *13*, 197. [CrossRef] [PubMed]
12. Floss, H.G.; Yu, T.W. Rifamycin—Mode of action, resistance, and biosynthesis. *Chem. Rev.* **2005**, *105*, 621–632. [CrossRef] [PubMed]
13. Campbell, E.A.; Korzheva, N.; Mustaev, A.; Murakami, K.; Nair, S.; Goldfarb, A.; Darst, S.A. Structural mechanism for rifampicin inhibition of bacterial RNA polymerase. *Cell* **2001**, *104*, 901–912. [CrossRef] [PubMed]
14. Wehrli, W. Rifampin: Mechanisms of action and resistance. *Rev. Infect. Dis.* **1983**, *5*, S407–S411. [CrossRef] [PubMed]
15. Ramirez, D.M.; Ramirez, D.; Arthur, G.; Zhanel, G.; Schweizer, F. Guanidinylated Polymyxins as Outer Membrane Permeabilizers Capable of Potentiating Rifampicin, Erythromycin, Ceftazidime and Aztreonam against Gram-Negative Bacteria. *Antibiotics* **2022**, *11*, 1277. [CrossRef] [PubMed]
16. Clinical and Laboratory Standards Institute. *Performance Standards for Antimicrobial Susceptibility Testing*, 35th ed.; CLSI Supplement M100; Clinical and Laboratory Standards Institute: Wayne, PA, USA, 2025.
17. European Committee on Antimicrobial Susceptibility Testing. Breakpoint Tables for Interpretation of MICs and Zone Diameters, Version 16.1; EUCAST: 2026. Available online: https://www.eucast.org/clinical_breakpoints/ (accessed on 24 November 2026).
18. Bisht, R.; Charlesworth, P.D.; Sperandeo, P.; Polissi, A. Breaking Barriers: Exploiting Envelope Biogenesis and Stress Responses to Develop Novel Antimicrobial Strategies in Gram-Negative Bacteria. *Pathogens* **2024**, *13*, 889. [CrossRef] [PubMed]
19. Wang, L.; Hu, C.; Shao, L. The antimicrobial activity of nanoparticles: Present situation and prospects for the future. *Int. J. Nanomed.* **2017**, *12*, 1227–1249. [CrossRef] [PubMed]
20. Stankic, S.; Suman, S.; Haque, F.; Vidic, J. Pure and multi metal oxide nanoparticles: Synthesis, antibacterial and cytotoxic properties. *J. Nanobiotechnol.* **2016**, *14*, 73. [CrossRef] [PubMed]
21. Khan, I.; Saeed, K.; Khan, I. Nanoparticles: Properties, applications and toxicities. *Arab. J. Chem.* **2019**, *12*, 908–931. [CrossRef]
22. Franco, D.; Calabrese, G.; Guglielmino, S.P.P.; Conoci, S. Metal-based nanoparticles: Antibacterial mechanisms and biomedical application. *Microorganisms* **2022**, *10*, 1778. [CrossRef] [PubMed]
23. Mammari, N.; Lamouroux, E.; Boudier, A.; Duval, R.E. Current knowledge on the oxidative-stress-mediated antimicrobial properties of metal-based nanoparticles. *Microorganisms* **2022**, *10*, 437. [CrossRef] [PubMed]
24. Singh, P.; Kim, Y.J.; Zhang, D.; Yang, D.C. Biological synthesis of nanoparticles from plants and microorganisms. *Biotechnol. Adv.* **2016**, *34*, 588–599. [CrossRef] [PubMed]
25. Iravani, S. Green synthesis of metal nanoparticles using plants. *Green Chem.* **2011**, *13*, 2638–2650. [CrossRef]
26. Bannunah, A.M. Biomedical applications of zirconia-based nanomaterials: Challenges and future perspectives. *Molecules* **2023**, *28*, 5428. [CrossRef] [PubMed]
27. Kathirvel, A.; Srinivasan, R.; Harini, S.; Ranjith, N.; Kumar, G.S.; Lalithambigai, K.; Atchudan, R.; Habila, M.A.; Aljuwayid, A.M.; Yun, H.K. Eco-friendly synthesis of zirconium dioxide nanoparticles from *Toddalia asiatica*: Applications in dye degradation, antioxidant and antibacterial activity. *Nanomaterials* **2025**, *15*, 84. [CrossRef] [PubMed]
28. da Silva, A.F.V.; Fagundes, A.P.; Macuvele, D.L.P.; de Carvalho, E.F.U.; Durazzo, M.; Padoin, N.; Soares, C.; Riella, H.G. Green synthesis of zirconia nanoparticles based on *Euclea natalensis* plant extract: Optimization of reaction conditions and evaluation of adsorptive properties. *Colloids Surf. A Physicochem. Eng. Asp.* **2019**, *583*, 123915. [CrossRef]
29. Aziz, S.N.; Al-Sallami, K.J.; Abd, S.Y.; Al-Musawi, A.M.A.; Mohammed, M.A.; Abed, A.-M.H.; Mohammed, S.Q. Improving the antibacterial activity by the combination of zirconium oxide nanoparticles (ZrO_2) and ceftazidime against *Klebsiella pneumoniae*. *Glob. J. Public Health Med.* **2019**, *1*, 16–20. [CrossRef]
30. Abd Algabar, F.A.; Ahmed, D.S.; Abbod, L.S.; Al-Obaidi, M.A. Antibacterial synergy: Assessing the impact of nano zirconium oxide particles in combination with selected antibiotics on *Escherichia coli* and *Klebsiella pneumoniae* isolates from urinary tract infections. *Indian J. Microbiol.* **2024**, *64*, 1894–1902. [CrossRef] [PubMed]
31. Catauro, M.; Barrino, F.; Dal Poggetto, G.; Milazzo, M.; Blanco, I.; Vecchio Ciprioti, S. Structure, drug absorption, bioactive and antibacterial properties of sol-gel SiO_2/ZrO_2 materials. *Ceram. Int.* **2020**, *46*, 29459–29465. [CrossRef]

32. Naskar, A.; Lee, S.; Lee, Y.; Kim, S.; Kim, K. A new nano-platform of erythromycin combined with Ag nano-particle ZnO nano-structure against methicillin-resistant *Staphylococcus aureus*. *Pharmaceutics* **2020**, *12*, 841. [CrossRef] [PubMed]
33. Sánchez-López, E.; Gomes, D.; Esteruelas, G.; Bonilla, L.; Lopez-Machado, A.L.; Galindo, R.; Cano, A.; Espina, M.; Ettcheto, M.; Camins, A.; et al. Metal-based nanoparticles as antimicrobial agents: An overview. *Nanomaterials* **2020**, *10*, 292. [CrossRef] [PubMed]
34. Tille, P.M. *Bailey & Scott's Diagnostic Microbiology*, 15th ed.; Elsevier: St. Louis, MO, USA, 2021.
35. Cappuccino, J.G.; Welsh, C.T. *Microbiology: A Laboratory Manual*, 12th ed.; Pearson: New York, NY, USA, 2020.
36. Lane, D.J. 16S/23S rRNA Sequencing. In *Nucleic Acid Techniques in Bacterial Systematics*; Stackebrandt, E., Goodfellow, M., Eds.; Wiley: New York, NY, USA, 1991; pp. 115–175.
37. Altschul, S.F.; Gish, W.; Miller, W.; Myers, E.W.; Lipman, D.J. Basic local alignment search tool. *J. Mol. Biol.* **1990**, *215*, 403–410. [CrossRef]
38. Williams, D.B.; Carter, C.B. *TEM: A Textbook for Materials Science*, 2nd ed.; Springer: New York, NY, USA, 2009.
39. Patterson, A.L. The Scherrer formula for X-ray particle size determination. *Phys. Rev.* **1939**, *56*, 978–982. [CrossRef]
40. Langford, J.I.; Wilson, A.J.C. Scherrer after sixty years: A survey and some new results. *J. Appl. Crystallogr.* **1978**, *11*, 102–113. [CrossRef]
41. Goldstein, J.I.; Newbury, D.E.; Michael, J.R.; Ritchie, N.W.M.; Scott, J.H.J.; Joy, D.C. *SEM and X-Ray Microanalysis*, 4th ed.; Springer: New York, NY, USA, 2018.
42. Odds, F.C. Synergy, antagonism, and what the chequerboard puts between them. *J. Antimicrob. Chemother.* **2003**, *52*, 1. [CrossRef] [PubMed]
43. Wasfi, R.; Elkhatib, W.F.; Ashour, H.M. Molecular typing and virulence analysis of MDR *Klebsiella pneumoniae* clinical isolates recovered from Egyptian hospitals. *Sci. Rep.* **2016**, *6*, 38929. [CrossRef] [PubMed]
44. Liu, Y.; Liu, C.; Zheng, W.; Zhang, X.; Yu, J.; Gao, Q.; Hou, Y.; Huang, X. PCR detection of *Klebsiella pneumoniae* in infant formula based on 16S–23S internal transcribed spacer. *Int. J. Food Microbiol.* **2008**, *125*, 230–235. [CrossRef] [PubMed]
45. Livak, K.J.; Schmittgen, T.D. Analysis of relative gene expression data using real-time quantitative PCR and the $2^{-\Delta\Delta Ct}$ method. *Methods* **2001**, *25*, 402–408. [CrossRef] [PubMed]
46. Blair, J.M.A.; Piddock, L.J.V. How to measure export via bacterial multidrug resistance efflux pumps. *mBio* **2016**, *7*, e00840-16. [CrossRef] [PubMed]
47. Paixão, L.; Rodrigues, L.; Couto, I.; Martins, M.; Fernandes, P.; de Carvalho, C.C.; Monteiro, G.A.; Sansonetty, F.; Amaral, L.; Viveiros, M. Fluorometric determination of EtBr efflux kinetics in *Escherichia coli*. *J. Biol. Eng.* **2009**, *3*, 18. [CrossRef] [PubMed]
48. French, G.L. Bactericidal agents in the treatment of MRSA infections: The potential role of daptomycin. *J. Antimicrob. Chemother.* **2006**, *58*, 1107–1117. [CrossRef] [PubMed]
49. Eaton, P.; Quaresma, P.; Soares, C.; Neves, C.; de Almeida, M.; Pereira, E.; West, P. A direct comparison of experimental methods to measure dimensions of synthetic nanoparticles. *Ultramicroscopy* **2017**, *182*, 179–190. [CrossRef] [PubMed]
50. Ghorbani, A.; Esmaeilizadeh, M. Pharmacological properties of *Salvia officinalis* and its components. *J. Tradit. Complement. Med.* **2017**, *7*, 433–440. [CrossRef] [PubMed]
51. Gowri, S.; Rajiv Gandhi, R.; Sundrarajan, M. Structural, optical, antibacterial and antifungal properties of zirconia nanoparticles prepared by a biobased protocol. *J. Mater. Sci. Technol.* **2014**, *30*, 782–790. [CrossRef]
52. Zhang, L.; Jiang, Y.; Ding, Y.; Daskalakis, N.; Jeuken, L.; Povey, M.; O'nEill, A.J.; York, D.W. Mechanistic investigation into antibacterial behaviour of suspensions of ZnO nanoparticles against *E. coli*. *J. Nanopart. Res.* **2010**, *12*, 1625–1636. [CrossRef]
53. Slavin, Y.N.; Asnis, J.; Häfeli, U.O.; Bach, H. Metal nanoparticles: Understanding the mechanisms behind antibacterial activity. *J. Nanobiotechnol.* **2017**, *15*, 65. [CrossRef] [PubMed]
54. Lemire, J.A.; Harrison, J.J.; Turner, R.J. Antimicrobial activity of metals: Mechanisms, molecular targets and applications. *Nat. Rev. Microbiol.* **2013**, *11*, 371–384. [CrossRef] [PubMed]
55. Hajipour, M.J.; Fromm, K.M.; Ashkarran, A.A.; de Aberasturi, D.J.; de Larramendi, I.R.; Rojo, T.; Serpooshan, V.; Parak, W.J.; Mahmoudi, M. Antibacterial properties of nanoparticles. *Trends Biotechnol.* **2012**, *30*, 499–511. [CrossRef] [PubMed]
56. Guruswamy Pandian, A.P.; Ramachandran, A.K.; Kodaganallur Pitchumani, P.; Mathai, B.; Thomas, D.C. Evaluation of anti-biofilm property of zirconium oxide nanoparticles on *Streptococcus mutans* and *Enterococcus faecalis*: An in vitro study. *Cureus* **2025**, *17*, e77199. [CrossRef] [PubMed]
57. Ferreira, L.; Pos, E.; Nogueira, D.R.; Ferreira, F.P.; Sousa, R.; Abreu, M.A. Antibiotics with antibiofilm activity—Rifampicin and beyond. *Front. Microbiol.* **2024**, *15*, 1435720. [CrossRef] [PubMed]
58. Li, Y.; Zhang, W.; Niu, J.; Chen, Y. Mechanism of photogenerated reactive oxygen species and correlation with the antibacterial properties of engineered metal-oxide nanoparticles. *ACS Nano* **2012**, *6*, 5164–5173. [CrossRef] [PubMed]

59. Sirelkhatim, A.; Mahmud, S.; Seeni, A.; Kaus, N.H.M.; Ann, L.C.; Bakhori, S.K.M.; Hasan, H.; Mohamad, D. Review on zinc oxide nanoparticles: Antibacterial activity and toxicity mechanism. *Nano-Micro Lett.* **2015**, *7*, 219–242. [CrossRef] [PubMed]
60. El-Demerdash, A.S.; Kamel, S.A.; Elariny, E.Y.T.; Henidi, H.; Mahran, Y.; Alahdal, H.; Saleh, A.M.; Ibrahim, R.A. Natural inhibitors of *Salmonella* MDR efflux pumps AcrAB and AcrD: An integrated in silico, molecular, and in vitro investigation. *Int. J. Mol. Sci.* **2024**, *25*, 12949. [CrossRef] [PubMed]

Disclaimer/Publisher's Note: The statements, opinions and data contained in all publications are solely those of the individual author(s) and contributor(s) and not of MDPI and/or the editor(s). MDPI and/or the editor(s) disclaim responsibility for any injury to people or property resulting from any ideas, methods, instructions or products referred to in the content.